Search for production of supersymmetric particles in final states with missing transverse momentum and multiple b-jets at $\sqrt{s}$ = 13 TeV proton-proton collisions with the ATLAS detector

The ATLAS Collaboration

24th March 2017

A search for supersymmetry involving the pair production of gluinos decaying via third-generation squarks to the lightest neutralino ($\tilde{\chi}_1^0$) is reported. It uses LHC proton–proton collision data at a centre-of-mass energy $\sqrt{s}$ = 13 TeV with an integrated luminosity of 36.1 fb^{-1} collected with the ATLAS detector in 2015 and 2016. The search is performed in events containing large missing transverse momentum and several energetic jets, at least three of which must be identified as originating from b-quarks. To increase sensitivity, the sample is divided depending on the presence or absence of electrons or muons. No excess is found above the predicted background. For $\tilde{\chi}_1^0$ masses below approximately 300 GeV, gluino masses of less than 1.97 (1.92) TeV are excluded at the 95% CL in simplified models involving the pair production of gluinos that decay via top (bottom) squark. An interpretation of the limits in terms of the branching ratios of the gluinos into third generation squarks is also provided. These results significantly extend the exclusion limits obtained with the 3.2 fb^{-1} of data collected in 2015.

1 Introduction

Supersymmetry (SUSY) [1–6] is a generalisation of space-time symmetries that predicts new bosonic partners to the fermions and new fermionic partners to the bosons of the Standard Model (SM). If R-parity is conserved [7], SUSY particles are produced in pairs and the lightest supersymmetric particle (LSP) is stable. The scalar partners of the left- and right-handed quarks, the squarks $\tilde{q}_L$ and $\tilde{q}_R$, can mix to form two mass eigenstates $\tilde{q}_1$ and $\tilde{q}_2$, ordered by increasing mass. SUSY can suppress the scale hierarchy [8–11] reducing unnatural tuning in the Higgs sector by orders of magnitude, provided that the superpartners of the top quark (stop, $\tilde{t}_1$ and $\tilde{t}_2$) have masses not too far above the weak scale. Because of the SM weak isospin symmetry, the mass of the left-handed bottom quark scalar partner (sbottom, $\tilde{b}_L$) is tied to the mass of the left-handed top quark scalar partner ($\tilde{t}_L$), and as a consequence the mass of the lightest sbottom $\tilde{b}_1$ is also expected to be close to the weak scale. The fermionic partners of the gluons, the gluinos ($\tilde{g}$), are also motivated by naturalness [12] to have a mass around the TeV scale in order to limit their contributions to the radiative corrections to the stop quark masses. For these reasons, and because the gluinos are expected to be pair-produced with a high cross-section at the Large Hadron Collider (LHC), the search for gluino production with decays via stop and sbottom quarks is highly motivated at the LHC.

This note presents the search for gluino pair production decaying via stop or sbottom quarks in events with multiple jets originating from the hadronisation of b-quarks (b-jets in the following), high missing transverse momentum of magnitude E_T^{miss}, and potentially additional light quark jets and/or an isolated charged lepton[1]. The dataset consists of 36.1 fb^{-1} of proton–proton collision data collected with the ATLAS detector [13] at a center-of-mass energy of 13 TeV in the years 2015 and 2016. Interpretations are provided in the context of several effective simplified models probing various gluino decays to third-generation squarks and the LSP. The latter is assumed to be the lightest neutralino $\tilde{\chi}_1^0$, a linear superposition of the superpartners of the neutral electroweak and Higgs bosons. The results supersede the ones obtained using 3.2 fb^{-1} of data collected in 2015 using the same strategy [14]. Pair-produced gluinos with stop-mediated decays have also been searched for using events containing pairs of same-sign leptons or three leptons in the 2015 ATLAS dataset [15]. The same-sign/three lepton search obtains comparable sensitivities to the search presented in this note when the masses of the gluino and the LSP are very close to each other. Similar searches performed in the CMS experiment using 13 TeV data [16–23] have produced comparable results to ATLAS searches.

2 SUSY signal models

Various simplified SUSY models [24, 25] are employed to optimize the event selection and/or interpret the results of the search. In terms of experimental signature, they all contain at least four b-jets originating from either gluino or top quark decays, and two $\tilde{\chi}_1^0$, which escape the detector unseen, resulting in high E_T^{miss}.

Gluinos are assumed to be pair-produced and to decay either as $\tilde{g} \to \tilde{b}_1 b$ or $\tilde{g} \to \tilde{t}_1 t$. The following stop and sbottom decays are then considered: $\tilde{t}_1 \to t\tilde{\chi}_1^0$, $\tilde{t}_1 \to b\tilde{\chi}_1^\pm$ and $\tilde{b}_1 \to b\tilde{\chi}_1^0$. In all cases, the stop

---

[1] The term "lepton" refers exclusively to an electron or a muon in this note.

or sbottom are assumed to be off-shell in order to have simplified models with only two parameters: the gluino and $\tilde{\chi}_1^0$ masses[2]. All other sparticles are decoupled.

Two simplified models are used to optimise the event selection in addition to interpreting the results. In the Gbb (Gtt) model, illustrated in Figure 1(a) (1(b)), each gluino undergoes an effective three-body decay $\tilde{g} \rightarrow b\bar{b}\tilde{\chi}_1^0$ ($\tilde{g} \rightarrow t\bar{t}\tilde{\chi}_1^0$) via off-shell sbottom (stop) quarks, with a branching ratio of 100%. The Gbb model is the simplest in terms of object multiplicity, resulting in the minimal common features of four b-jets and two $\tilde{\chi}_1^0$. In addition to these objects, the Gtt model produces four W bosons originating from the top quark decays: $t \rightarrow Wb$. The presence of these four W bosons motivates the design of signal regions with a higher jet multiplicity than for Gbb models, and in some cases with at least one isolated electron or muon.
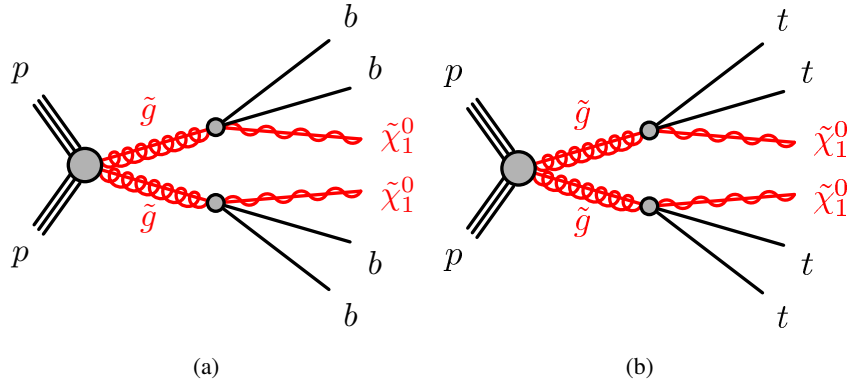

Figure 1: The decay topologies in the (a) Gbb and (b) Gtt simplified models.

This note includes a novel interpretation that probes the sensitivity of the search as a function of the gluino branching ratio, in addition to the gluino and $\tilde{\chi}_1^0$ masses. For that interpretation a third gluino decay is considered: $\tilde{g} \rightarrow tb\tilde{\chi}_1^\pm$ (via the off-shell stop decay $\tilde{t}_1 \rightarrow b\tilde{\chi}_1^\pm$). The $\tilde{\chi}_1^\pm$ is then forced to decay as $\tilde{\chi}_1^\pm \rightarrow W^*\tilde{\chi}_1^0 \rightarrow f\bar{f}'\tilde{\chi}_1^0$ (where f stands for a fermion). To keep the numbers of model parameters at only two, the mass difference between the $\tilde{\chi}_1^\pm$ and the $\tilde{\chi}_1^0$ is fixed to 2 GeV. Such a small mass splitting between the $\tilde{\chi}_1^\pm$ and the $\tilde{\chi}_1^0$ is typical of models where the $\tilde{\chi}_1^0$ is Higgsino-like (see e.g. Ref. [27]), which are well motivated by naturalness. Consequently, the products of the decay $W^* \rightarrow f\bar{f}'$ are typically too soft to be detected, except for very large mass differences between the gluino and the $\tilde{\chi}_1^\pm$. Thus, in this model, the gluino can decay as either $\tilde{g} \rightarrow b\bar{b}\tilde{\chi}_1^0$, $\tilde{g} \rightarrow tb\tilde{\chi}_1^\pm$ (with $\tilde{\chi}_1^\pm \rightarrow f\bar{f}'\tilde{\chi}_1^0$) or $\tilde{g} \rightarrow t\bar{t}\tilde{\chi}_1^0$, with the sum of individual branching ratios adding up to 100%. This model probes more realistic scenarios where the branching ratio to either $\tilde{g} \rightarrow b\bar{b}\tilde{\chi}_1^0$ or $\tilde{g} \rightarrow t\bar{t}\tilde{\chi}_1^0$ is not 100%, and where one, two or three top quarks, and thus on-shell W bosons, are possible in the final state, in-between the Gbb (no top quarks) and Gtt (four top quarks) decay topologies. The decay topologies that are considered in the variable branching ratio model are illustrated in Figure 2. The model also includes the Gbb and Gtt decay topologies illustrated in Figure 1. A limited set of 10 mass points are generated for this variable branching ratio model with $m_{\tilde{g}}$ varying from 1.5 TeV to 2.3 TeV and $m_{\tilde{\chi}_1^0}$ varying from 1 GeV to 1 TeV.

The technical implementation of the simulated samples produced from these models is described in Section 4.

---

[2] Models with on-shell sbottom and stop were studied in Run 1 [26] and the limits on the gluino and the $\tilde{\chi}_1^0$ masses were found to be mostly independent of the stop and sbottom masses, except when the stop is very light.
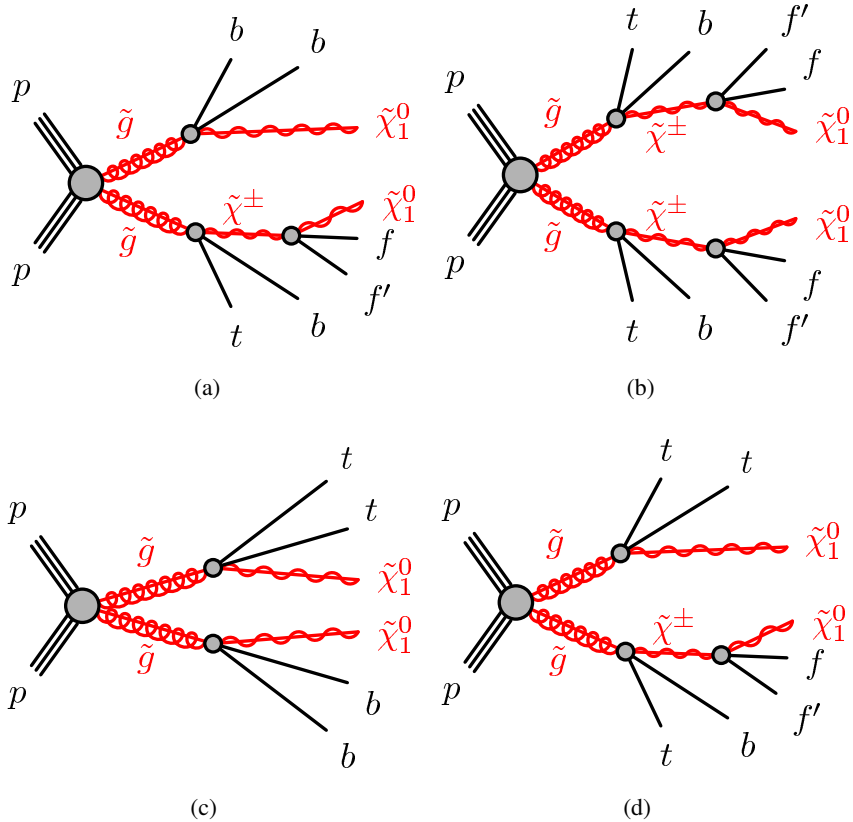
Figure 2: The additional decay topologies of the varying gluino branching ratio model in addition to the ones of Figure 1. The fermions originating from the $\tilde{\chi}_1^\pm$ decay are typically soft because the mass difference between the $\tilde{\chi}_1^\pm$ and the $\tilde{\chi}_1^0$ is fixed to 2 GeV.

3 ATLAS detector

The ATLAS detector is a multipurpose particle physics detector with a forward-backward symmetric cylindrical geometry and nearly 4π coverage in solid angle.[3] The inner tracking detector (ID) consists of silicon pixel and microstrip detectors covering the pseudorapidity region $|\eta| < 2.5$, surrounded by a transition radiation tracker, which enhances electron identification in the region $|\eta| < 2.0$. Before the start of Run 2, the new innermost pixel layer, the Insertable B-Layer (IBL) [28], was inserted at a mean sensor radius of 3.3 cm. The ID is surrounded by a thin superconducting solenoid providing an axial 2 T magnetic field and by a fine-granularity lead/liquid-argon (LAr) electromagnetic calorimeter covering $|\eta| < 3.2$. A steel/scintillator-tile calorimeter provides coverage for hadronic showers in the central pseudorapidity range ($|\eta| < 1.7$). The endcaps ($1.5 < |\eta| < 3.2$) of the hadronic calorimeter are made of LAr active layers with either copper or tungsten as the absorber material. The forward region ($3.1 < |\eta| < 4.9$) is instrumented with a LAr calorimeter for both EM and hadronic measurements. A muon spectrometer with an air-core toroid magnet system surrounds the calorimeters. Three layers of high-precision tracking

---

[3] ATLAS uses a right-handed coordinate system with its origin at the nominal interaction point in the centre of the detector. The positive x-axis is defined by the direction from the interaction point to the center of the LHC ring, with the positive y-axis pointing upwards, while the beam direction defines the z-axis. Cylindrical coordinates (r, ϕ) are used in the transverse plane, ϕ being the azimuthal angle around the z-axis. The pseudorapidity η is defined in terms of the polar angle θ by $\eta = -\ln\tan(\theta/2)$.

chambers provide coverage in the range $|\eta| < 2.7$, while dedicated fast chambers allow triggering in the region $|\eta| < 2.4$. The ATLAS trigger system [29] consists of a hardware-based Level-1 trigger (L1) followed by a software-based High Level Trigger (HLT).

4 Data and simulated event samples

The data used in this analysis were collected by the ATLAS detector from pp collisions produced by the LHC at a centre-of-mass-energy of 13 TeV and 25 ns proton bunch spacing over the 2015 and 2016 data-taking periods. The full dataset corresponds to an integrated luminosity of 36.1 fb^{-1} after requiring that all detector subsystems were operational during data recording. The uncertainty in the combined 2015+2016 integrated luminosity is 3.2%. It is derived, following a methodology similar to that detailed in Ref. [30], from a preliminary calibration of the luminosity scale using x–y beam-separation scans performed in August 2015 and May 2016. Events are required to pass an E_T^{miss} trigger [31] with lower thresholds of 70 GeV, 100 GeV and 110 GeV at the HLT level for the 2015, early and late 2016 datasets, respectively. These triggers are fully efficient for events passing the preselection defined in Section 6, which requires the offline reconstructed E_T^{miss} to exceed 200 GeV. There are on average 13.7 and 24.9 inelastic pp collisions ("pileup") in the same bunch crossing in the 2015 and 2016 data, respectively.

Simulated event samples are used to model the signal and background processes in this analysis, except multijet processes which are estimated from data. SUSY signal samples in which each gluino decays to $bb\tilde{\chi}_1^0$, $tt\tilde{\chi}_1^0$, or $tb\tilde{\chi}_1^0$ are generated with up to two additional partons using MADGRAPH5_aMC@NLO [32] v2.2.2 at leading order (LO) with NNPDF 2.3 [33] parton density function (PDF) sets. These samples are interfaced to PYTHIA v8.186 [34] for the modelling of the parton showering, hadronisation and underlying event.

The dominant background in the signal regions is the production of $t\bar{t}$ pairs with additional high transverse momentum (p_T) jets. For the generation of $t\bar{t}$ and single top-quarks in the Wt- and s-channels the POWHEG-BOX [35] v2 generator with the CT10 [36] PDF sets in the matrix element calculations is used. Electroweak t-channel single top-quark events are generated using the POWHEG-BOX v1 generator. This generator uses the four-flavour scheme for the NLO matrix elements calculations together with the fixed four-flavour PDF set CT10f4. For all processes involving top quarks, top-quark spin correlations are preserved. In the t-channel, top quarks are decayed using MadSpin [37]. The parton shower, fragmentation, and the underlying event are simulated using PYTHIA 6.428 [38] with the CTEQ6L1 PDF sets. The h_{damp} parameter in POWHEG, which controls the p_T of the first additional emission beyond the Born level and thus regulates the p_T of the recoil emission against the $t\bar{t}$ system, is set to the mass of the top quark (m_{top} = 172.5 GeV). All events with at least one leptonically decaying W boson are included. Fully hadronic $t\bar{t}$ and single top events do not contain sufficient E_T^{miss} to contribute significantly to the background.

Smaller backgrounds in the signal region come from the production of $t\bar{t}$ pairs in association with $W/Z/h$ bosons and possibly additional jets, production of $t\bar{t}t\bar{t}$, W/Z+jets and $WW/WZ/ZZ$ (diboson) events. Other potential source of backgrounds, such as the production of three top quarks or three gauge bosons, are expected to be negligible. The production of $t\bar{t}$ pairs in association with electroweak vector bosons W and Z are modeled by samples generated at LO using MADGRAPH5_aMC@NLO v2.2.2 and showered with PYTHIA v8.186, while samples to model $t\bar{t}H$ production are generated using MAD-GRAPH5_aMC@NLO v2.2.1 and showered with HERWIG++ [39] v2.7.1. These samples are described in detail in Ref. [40]. MADGRAPH5_aMC@NLO is also used to simulate the $t\bar{t}t\bar{t}$ production and the shower-ing is performed with PYTHIA v8.186. W/Z+jets processes are simulated using the SHERPA v2.2 [41]

generator, while SHERPA v2.1.1 is used to simulate diboson production processes. Matrix elements for the W/Z+jets and diboson processes are calculated using the Comix [42] and OpenLoops [43] generators and merged with the SHERPA parton shower [44] using the ME+PS@NLO prescription [45]. The SHERPA diboson sample cross section has been scaled down to account for its use of α_{QED}=1/129 rather than 1/132, corresponding to the use of current PDG parameters, as input to the G_μ scheme [46]. Samples generated using MADGRAPH5_aMC@NLO v2.2.2 are produced with NNPDF 2.3 PDF sets, while all other samples are generated with CT10 PDFs.

For all samples, except the ones generated using SHERPA, the EVTGEN v1.2.0 program [47] is used to simulate the properties of the bottom and charm-hadron decays. All PYTHIA v6.428 samples use the PERUGIA2012 (P2012) [48] set of tuned parameters (tune) for the underlying event, while PYTHIA v8.186 and HERWIG++ showering are run with the A14 [49] and UEEE5 [50] underlying-event tunes, respectively. In-time and out-of-time pileup interactions from the same or nearby bunch-crossings are simulated by overlaying additional pp collisions generated by PYTHIA v8.186, using the A2MSTW2008LO underlying-event tune [51], on top of the hard-scattering events. Details of the sample generation and normalization are summarized in Table 1. Additional samples with different generators and settings are used to estimate systematic uncertainties on the backgrounds, as described in Section 8.

All simulated event samples are passed through the full ATLAS detector simulation using GEANT4 [52], with the exception of signal samples in which both gluinos do not only decay to $tt\tilde{\chi}_1^0$, which are passed through a fast simulation that uses a parameterised description to simulate the response of the calorimeter systems [53]. The simulated events are reconstructed with the same algorithm as that used for data.

The signal samples are normalised using the best cross-sections calculated at NLO in the strong coupling constant, adding the resummation of soft gluon emission at next-to-leading-logarithmic (NLL) accuracy [54–58]. The nominal cross-section and the uncertainty are taken from an envelope of cross-section predictions using different PDF sets and factorisation and renormalisation scales, as described in Ref. [59]. The cross-section of gluino pair-production in these simplified models is (14 ± 3) fb for a gluino mass of 1.5 TeV, falling to (1.0 ± 0.3) fb for 2 TeV mass gluinos. All background processes are normalised to the best available theoretical calculation for their respective cross-sections. The order of this calculation in perturbative QCD (pQCD) for each process is listed in Table 1.

Finally, contributions from multijet background are estimated from data using a procedure described in [60], which perfoms the smearing of the jet response in data events with well-measured E_T^{miss} (so-called "seed events"). The response function is derived in MC dijet events and is different for b-tagged and non-b-tagged jets.

5 Object reconstruction

Interaction vertices from the proton–proton collisions are reconstructed from at least two tracks with $p_T > 0.4$ GeV, and are required to be consistent with the beamspot envelope. The primary vertex is identified as the one with the largest sum of squares of the transverse momenta from associated tracks $(\sum |p_{T,track}|^2)$ [67].

Basic selection criteria are applied to define candidates for electrons, muons and jets in the event. An overlap removal procedure is applied to these candidates to prevent double-counting. Further requirements are then made to select the final signal leptons and jets from the remaining objects. The details of the object selections and of the overlap removal procedure are given below.

Process	Generator + fragmentation/hadronization	Tune	PDF set	Cross-section order
SUSY signal	MadGraph5_aMC@NLO v2.2.2 + Pythia v8.186	A14	NNPDF2.3	NLO+NLL [54–59]
$t\bar{t}$	Powheg-Box v2 + Pythia v6.428	PERUGIA2012	CT10	NNLO+NNLL [61]
Single top	Powheg-Box v1 or v2 + Pythia v6.428	PERUGIA2012	CT10	NNLO+NNLL [62–64]
$t\bar{t}W/t\bar{t}Z$/**4-tops**	MadGraph5_aMC@NLO v2.2.2 + Pythia v8.186	A14	NNPDF2.3	NLO [32]
$t\bar{t}H$	MadGraph5_aMC@NLO v2.2.1 + Herwig++ v2.7.1	UEEE5	CT10	NLO [65]
Diboson WW, WZ, ZZ	Sherpa v2.1.1	Default	CT10	NLO [46]
W/Z+jets	Sherpa v2.2	Default	CT10	NNLO [66]

Table 1: List of generators used for the different processes. Information is given about the underlying-event tunes, the PDF sets and the pQCD highest-order accuracy used for the normalization of the cross-section the different samples.

Candidate jets are reconstructed from three-dimensional topological energy clusters [68] in the calorimeter using the anti-k_t jet algorithm [69] with a radius parameter of 0.4 (small-R jets). Each topological cluster is calibrated to the electromagnetic scale response prior to jet reconstruction [70]. The reconstructed jets are then calibrated to the particle level by the application of a jet energy scale (JES) derived from $\sqrt{s}$ = 13 TeV data and simulations [71]. Quality criteria are imposed to reject events that contain at least one jet arising from non-collision sources or detector noise [72]. Further selections are applied to reject jets that originate from pileup interactions by the means of a multivariate algorithm using the information about the tracks matched to each jet [73]. Candidate jets are required to have $p_T > 20$ GeV and $|\eta| < 2.8$. After resolving overlaps with electrons and muons, selected jets are required to satisfy the stricter requirement of $p_T > 30$ GeV.

A jet is tagged as a b-jet by means of a multivariate algorithm using information about the impact parameters of inner detector tracks matched to the jet, the presence of displaced secondary vertices, and the reconstructed flight paths of b- and c-hadrons inside the jet [74, 75]. The b-tagging working point corresponding to an efficiency of 77% to identify b-jets with $p_T > 20$ GeV, as determined from a sample of simulated $t\bar{t}$ events, was found to be optimal for this search. The corresponding rejection factors against jets originating from c-quarks, from τ-leptons and from light quarks and gluons in the same sample at this working point are 6, 22 and 134, respectively.

After resolving the overlap with leptons, the candidate small-R jets are re-clustered [76] into large-R jets using the anti-k_t algorithm with a radius parameter of 0.8. The calibration from the input small-R jets propagates directly to the re-clustered jets. These re-clustered jets are then trimmed [76–79] by removing subjets whose p_T falls below 10% of the p_T of the original re-clustered jet. The resulting large-R jets are required to have $p_T > 100$ GeV and $|\eta| < 2.0$. When it is not explicitly stated otherwise, the term "jets" in this note refers to small-R jets.

Electron candidates are reconstructed from energy clusters in the electromagnetic calorimeter and inner detector tracks and are required to satisfy a set of "loose" quality criteria [80, 81]. They are also required to have $|\eta| < 2.47$. Muon candidates are reconstructed from matching tracks in the inner detector and in the muon spectrometer. They are required to meet "medium" quality criteria, as described in Ref. [82], and to have $|\eta| < 2.5$. All electron and muon candidates must have $p_T > 20$ GeV. Leptons are selected from the candidates that survive the overlap removal procedure if they fulfill a requirement on the scalar sum of p_T of additional inner detector tracks in a cone around the lepton track. This isolation requirement is defined to ensure a flat efficiency of around 99% across the whole electron transverse energy and muon transverse momentum ranges. The angular separation between the lepton and the b-jet ensuing from a semi-leptonic top quark decay narrows as the p_T of the top quark increases. This increased collimation is accounted for by setting the radius of the isolation cone to min(0.2, 10 GeV/p_T^{lep}), where p_T^{lep} is the lepton p_T expressed in GeV. Selected electrons are further required to meet the "tight" quality criteria [80, 81]. Electrons (muons) are matched to the primary vertex by requiring the transverse impact parameter d_0 of the associated ID track to satisfy $|d_0|/\sigma_{d_0} < 5$ (3), where σ_{d_0} is the measured uncertainty of d_0, and the longitudinal impact parameter z_0 to satisfy $|z_0 \sin\theta| < 0.5$ mm[4]. In addition, events containing one or more muon candidates with $|d_0|$ ($|z_0|$) > 0.2 mm (1 mm) are rejected to suppress cosmic rays.

Overlaps between candidate objects are removed sequentially. Firstly, electron candidates that lie within $\Delta R < 0.01$[5] from muon candidates are removed to suppress contributions from muon bremsstrahlung. Overlaps between electron and jet candidates are resolved next, and finally, overlaps between remaining jets and muon candidates are removed.

Overlap removal between electron and jet candidates aims to resolve two sources of ambiguity: it is designed, firstly, to remove jets that are formed primarily from the showering of a prompt electron and, secondly, to remove electrons that are produced in the decay chains of hadrons. Consequently, any non-b-tagged jet whose axis lies within $\Delta R < 0.2$ from an electron is discarded. Electrons with $E_T < 50$ GeV are discarded if they lie within $\Delta R < 0.4$ to the axis of any remaining jet and the corresponding jet is kept. For higher-E_T electrons, the latter removal is performed using a threshold of $\Delta R = \min(0.4, 0.04 + 10\,\text{GeV}/E_T)$ to increase the acceptance for events with collimated top quark decay.

The overlap removal procedure between muon and jet candidates is designed to remove those muons that are likely to have originated from the decay of hadrons and to retain the overlapping jet. Jets and muons may also appear in close proximity when the jet results from high-p_T muon bremsstrahlung, and in such cases the jet should be removed and the muon retained. Such jets are characterized by having very few matching inner detector tracks. Therefore, if the angular distance ΔR between a muon and a jet is lower than 0.2, the jet is removed if it is not b-tagged and has fewer than three matching inner detector tracks. As for the electrons, muons with p_T below (above) 50 GeV are subsequently discarded if they lie within $\Delta R = 0.4$ ($\Delta R = \min(0.4, 0.04 + 10\,\text{GeV}/p_T)$) of any remaining jet.

The missing transverse momentum (E_T^{miss}) in the event is defined as the magnitude of the negative vector sum ($\vec{p}_T^{\text{miss}}$) of the transverse momenta of all selected and calibrated objects in the event, with an extra term added to account for energy deposits that are not associated to any of these selected objects. This "soft" term is calculated from inner detector tracks matched to the primary vertex to make it more resilient to contamination from pileup interactions [83, 84].

---

[4] Both transverse and longitudinal impact parameters are defined with respect to the selected primary vertex.

[5] $\Delta R = \sqrt{(\Delta y)^2 + (\Delta\phi)^2}$ defines the distance in rapidity y and azimuthal angle ϕ.

Corrections derived from data control samples are applied to simulated events to account for differences between data and simulation in the reconstruction efficiencies, momentum scale and resolution of leptons, in the efficiency and false positive rate for identifying b-jets, and in the efficiency for rejecting jets originating from pileup interactions.

6 Event preselection

The event selection criteria are defined based on kinematic requirements on the objects defined in Section 5 and on the following event variables.

The effective mass variable (m_{eff}) is defined as:

$$m_{\text{eff}} = \sum_i p_{\text{T}}{}^{\text{jet}_i} + \sum_j p_{\text{T}}^{\ell_j} + E_{\text{T}}^{\text{miss}},$$

where the first and second sums are over the selected jets (N_{jet}) and leptons (N_{lepton}), respectively. It typically has a much higher value in pair-produced gluino events than in background events.

In regions with at least one selected lepton, the transverse mass m_{T} composed of the p_{T} of the leading selected lepton (ℓ) and $E_{\text{T}}^{\text{miss}}$ is defined as:

$$m_{\text{T}} = \sqrt{2p_{\text{T}}^{\ell} E_{\text{T}}^{\text{miss}}\{1 - \cos[\Delta\phi(\vec{p}_{\text{T}}^{\text{miss}}, \vec{p}_{\text{T}}^{\ell})]\}}.$$

It is used to discriminate between the signal and backgrounds from semi-leptonic $t\bar{t}$ and W+jets events. Neglecting resolution effects, the m_{T} distribution for these backgrounds is bounded from above by the W boson mass and typically has higher values for Gtt events. Another useful transverse mass variable is $m_{\text{T,min}}^{b\text{-jets}}$, the minimum transverse mass formed by $E_{\text{T}}^{\text{miss}}$ and any of the three highest-p_{T} b-tagged jets in the event:

$$m_{\text{T,min}}^{b\text{-jets}} = \min_{i \leq 3}\left(\sqrt{2p_{\text{T}}^{b\text{-jet}_i} E_{\text{T}}^{\text{miss}}\{1 - \cos[\Delta\phi(\vec{p}_{\text{T}}^{\text{miss}}, \vec{p}_{\text{T}}^{b\text{-jet}_i})]\}}\right).$$

It is bounded from above by the top quark mass for semi-leptonic $t\bar{t}$ events, while peaking at higher values for Gbb and Gtt events.

The total jet mass variable is defined as:

$$M_J^{\Sigma} = \sum_{i \leq 4} m_{J,i},$$

where $m_{J,i}$ is the mass of the large-radius re-clustered jet i in the event. The decay products of a hadronically-decaying boosted top quarks can be reconstructed in a single large-radius re-clustered jet, resulting in a jet with a high mass. This variable will typically have larger values for Gtt events, which contain as much as four hadronically-decaying top quarks, then background, which is dominated by semi-leptonic and di-leptonic $t\bar{t}$ events.

The requirement of a selected lepton, with the additional requirements on jets, $E_{\text{T}}^{\text{miss}}$ and event variables described in Section 7, makes the multijet background negligible for the $\geq$ 1-lepton signal regions. For

9

the 0-lepton signal regions, the minimum azimuthal angle between $\vec{p}_{\mathrm{T}}^{\mathrm{miss}}$ and the p_{T} of the leading four small-R jets in the event, denoted $\Delta\phi_{\mathrm{min}}^{4\mathrm{j}}$, defined as:

$$\Delta\phi_{\mathrm{min}}^{4\mathrm{j}} = \min_{i \leq 4} \left(|\phi_{\mathrm{jet}_i} - \phi_{\vec{p}_{\mathrm{T}}^{\mathrm{miss}}}| \right),$$

is required to be greater than 0.4. This requirement ensures that the multijet background, which can produce events with large $E_{\mathrm{T}}^{\mathrm{miss}}$ if containing poorly measured jets or neutrinos emitted close to the axis of a jet, is also negligible in most of the 0-lepton signal regions (along with the other requirements on jets, $E_{\mathrm{T}}^{\mathrm{miss}}$ and event variables described in Section 7).

A similar variable, denoted $\Delta\phi^{\mathrm{j1}}$ is also used in the Gbb signal regions targeting small mass differences between the gluino and the neutralino, allowing for the identification of events containing a high-p_{T} jet coming from initial state radiation (ISR) and recoiling against the gluino pair. It is defined as the absolute value of the azimutal angle separating the p_{T} of the leading jet and $\vec{p}_{\mathrm{T}}^{\mathrm{miss}}$, and is expected to have larger values for the targeted signal than for the background.

Preselection criteria in the 0-lepton and 1-lepton channels are defined in Table 2. They require $E_{\mathrm{T}}^{\mathrm{miss}} > 200$ GeV, in addition to the $E_{\mathrm{T}}^{\mathrm{miss}}$ trigger requirement, and at least four jets of which at least two must be b-tagged. The 0-lepton channel has a veto on the number of selected leptons, and the 1-lepton channel requires at least one selected lepton.

	Preselection requirements	
	0-lepton	1-lepton
Trigger	$E_{\mathrm{T}}^{\mathrm{miss}}$ trigger	
$E_{\mathrm{T}}^{\mathrm{miss}}$	$E_{\mathrm{T}}^{\mathrm{miss}} > 200$ GeV	
N_{lepton}	$= 0$	≥ 1
$\Delta\phi_{\mathrm{min}}^{4\mathrm{j}}$	> 0.4	$-$
N^{jet}	≥ 4	
$N^{b-\mathrm{tag}}$	≥ 2	

Table 2: Definition of the preselection criteria.

Correction factors are extracted to account for shape discrepancies in the m_{eff} spectrum between the data and background expectations for the 1-lepton preselection sample. These factors are defined as the ratio of the number of observed events to the predicted number of background events in a given m_{eff} bin, in a signal-depleted region. This region is defined by the 1-lepton preselection criteria plus requiring exactly two b-tagged jets and $m_{\mathrm{T,min}}^{b\text{-jets}} < 140$ GeV. This kinematic reweighting leads to correction factors ranging from 0.7 to 1.1. They are applied to the background prediction and the full size of the correction is taken as an uncertainty for both the background and signal events.

Figures 3 and 4 show the multiplicity of selected jets and b-jets, and the distributions for $E_{\mathrm{T}}^{\mathrm{miss}}$, m_{eff}, M_J^{Σ} for events passing the 0-lepton or the 1-lepton preselection, respectively. Figure 3 (4) also displays the distribution of $m_{\mathrm{T,min}}^{b\text{-jets}}$ (m_{T}) in the 0-lepton (1-lepton) channel. The correction described above is applied in the

1-lepton channel. The uncertainty bands include the statistical and experimental systematic uncertainties, as described in Section 8, but not the theoretical uncertainties on the background modelling.

The agreement between data and background prediction is found to be reasonable at the preselection level after the kinematic reweighting described above. A discrepancy between data and expectation is observed for the number of b-tagged jets, but it has a negligible impact on the background estimate after the renormalization of the simulation in dedicated control regions with the same b-tagged jets requirements as the signal regions, as described in Section 7. Example signal models with enhanced cross-sections are overlaid for comparison.

7 Analysis strategy

In order to enhance sensitivity to the various signal benchmarks described in Section 2, multiple signal regions (SRs) are designed. The main background source in all these regions is the associated production of a $t\bar{t}$ pair together with heavy and light flavour jets. While the normalisation of non-$t\bar{t}$ backgrounds is taken from the theory prediction, the $t\bar{t}$ normalisation for each individual SR is extracted from a data control region (CR) that has comparable background composition and kinematics. This is ensured by keeping similar kinematic requirements between both regions, and exactly the same selection on $N_{b\text{-jets}}$. CRs and SRs are defined to be mutually exclusive. Signal contribution in the CRs is suppressed by reverting or relaxing some requirements on the kinematic variables (e.g. m_T, $m_{T,\min}^{b\text{-jets}}$), leading to a signal contamination in the CRs of 6% at most. The $t\bar{t}$ normalisation is cross-checked in validation regions (VRs) that share similar background composition, i.e. jet and lepton flavours, with the SR. The signal contamination in the VRs has been checked to be lower than 30% for benchmark signal mass points above the already excluded mass range.

Two analysis strategies are followed, and different SR sets are defined for each:

- a **cut-and-count** analysis, using partially-overlapping single-bin SRs, optimised to maximise the expected discovery power for benchmark signal models and being easily recastable. The SRs are defined to probe the existence of a signal or to assess model-independent upper limits on the number of signal events;

- a **multi-bin** analysis, using a set of non-overlapping SRs and CRs that are combined together to strengthen the exclusion limits on the targeted signal benchmarks. This set of regions is used to assess model-dependent interpretations of the various signal models.

7.1 Cut-and-count analysis

SRs targeting the Gtt model in the 1-lepton channel are presented in Table 3. The region labelled A is optimised for signals with a large mass difference (Δm) between the gluino and the neutralino (Δm $\gtrsim$ 1.5 TeV), possibly leading to highly boosted objects in the final state. Conversely, region C primarily focuses on signals for which the gluino decay products are softer due to the small Δm (Δm $\lesssim$ 300 GeV). Region B targets intermediate values of Δm. As can be seen from Table 3 these regions differ mainly in their kinematic selections thresholds: m_{eff}, E_T^{miss} and M_J^Σ selections are relaxed when going from region A to C to improve the acceptance for softer signals. The resulting background increase is compensated by tightening the requirements on the number of (b-tagged) jets or $m_{T,\min}^{b\text{-jets}}$.
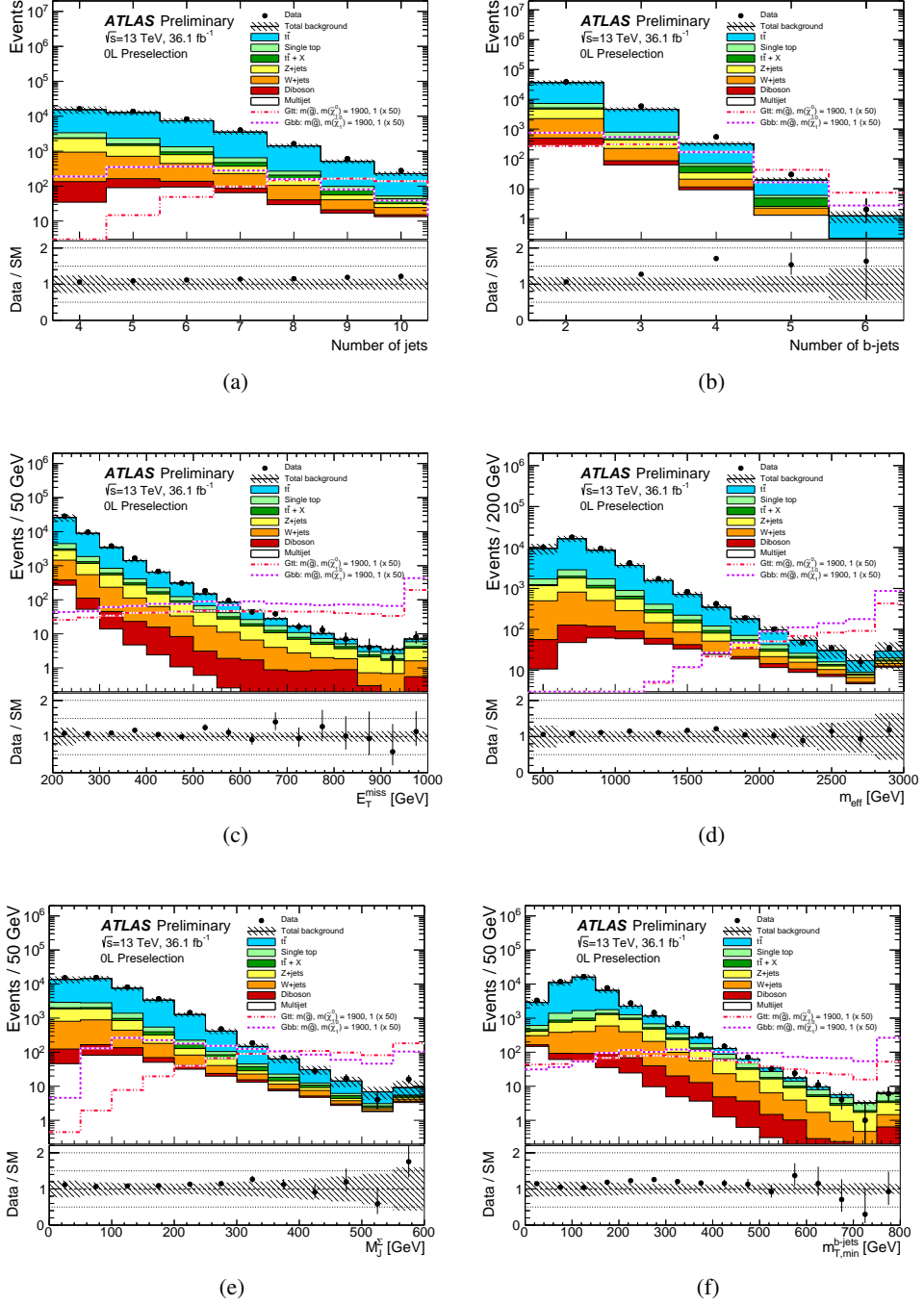
Figure 3: Distributions of (a) the number of selected jets (N_{jet}), (b) the number of selected b-jets, (c) E_T^{miss}, (d) m_{eff}, (e) M_J^{Σ} and (f) $m_{T,\text{min}}^{b\text{-jets}}$ for events passing the 0-lepton preselection criteria. The statistical and experimental systematic uncertainties (as defined in Section 8) are included in the uncertainty band. The last bin includes overflows. The lower part of each figure shows the ratio of data to the background prediction. All backgrounds (including $t\bar{t}$) are normalized using the best available theoretical calculation described in Section 4. The background category $t\bar{t} + X$ includes $t\bar{t}W/Z$, $t\bar{t}h$ and $t\bar{t}t\bar{t}$ events. Example signal models with cross-sections enhanced by a factor of 50 are overlaid for comparison.
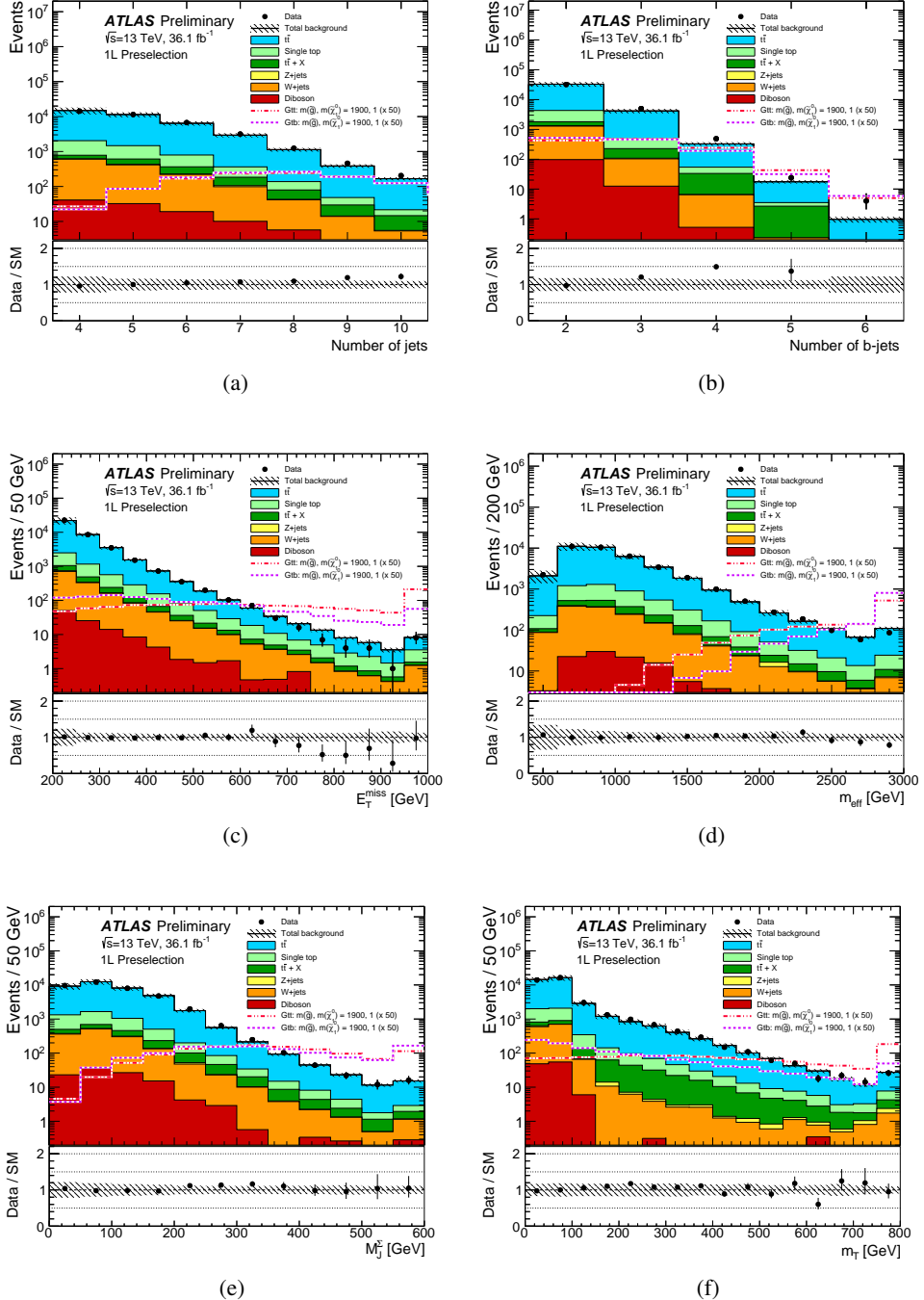
Figure 4: Distributions of (a) the number of selected jets (N_{jet}), (b) the number of selected b-jets, (c) E_T^{miss}, (d) m_{eff}, (e) M_J^Σ and (f) m_T for events passing the 1-lepton preselection criteria, after applying the kinematic reweighting to the m_{eff} distribution described in the text (which has been performed with a different binning than the m_{eff} figure presented here). The statistical and experimental systematic uncertainties (as defined in Section 8) are included in the uncertainty band. The last bin includes overflows. The lower part of each figure shows the ratio of data to the background prediction. All backgrounds (including $t\bar{t}$) are normalized using the best available theoretical calculation described in Section 4. The background category $t\bar{t} + X$ includes $t\bar{t}W/Z$, $t\bar{t}h$ and $t\bar{t}t\bar{t}$ events. Example signal models with cross-sections enhanced by a factor of 50 are overlaid for comparison.

13

CRs constraining the $t\bar{t}$ background are defined in the low m_{T} region to remove overlaps with the SRs. The requirements on $m_{\mathrm{T,min}}^{b\text{-jets}}$ are removed, and the selections on kinematic variables are relaxed to ensure around at least 10 events in all CRs.

The requirement of an exclusive jet multiplicity permits the definition of VRs kinematically close to the SRs and mutually exclusive to both the CRs and SRs. VR-m_{T} validates the background prediction in the high-m_{T} region. It is kept mutually exclusive with the SR thanks to an inverted selection on M_J^{Σ} or $m_{\mathrm{T,min}}^{b\text{-jets}}$. VR-$m_{\mathrm{T,min}}^{b\text{-jets}}$ checks the background prediction in the high-$m_{\mathrm{T,min}}^{b\text{-jets}}$ regime, with an upper cut on m_{T} to keep the region mutually exclusive with the corresponding SR. The other kinematic requirements are kept as close as possible to those of the SRs to maintain the event kinematics similar to those in the SR, and allow sufficiently large yields.

	Criteria common to all Gtt 1-lepton regions		
	≥ 1 signal lepton, $p_{\mathrm{T}}^{\text{jet}} > 30$ GeV, $N_{b\text{-jets}} \geq 3$		
	Variable	SR	CR
	N_{jet}	≥ 5	$= 5$
	m_{T}	> 150	< 150
Region A	$m_{\mathrm{T,min}}^{b\text{-jets}}$	> 120	–
(Large Δm)	$E_{\mathrm{T}}^{\text{miss}}$	> 500	> 300
	$m_{\text{eff}}^{\text{incl}}$	> 2200	> 1700
	M_J^{Σ}	> 200	> 150
	N_{jet}	≥ 6	$= 6$
	m_{T}	> 150	< 150
Region B	$m_{\mathrm{T,min}}^{b\text{-jets}}$	> 160	–
(Moderate Δm)	$E_{\mathrm{T}}^{\text{miss}}$	> 450	> 400
	$m_{\text{eff}}^{\text{incl}}$	> 1800	> 1500
	M_J^{Σ}	> 200	> 100
	N_{jet}	≥ 7	$= 7$
	m_{T}	> 150	< 150
Region C	$m_{\mathrm{T,min}}^{b\text{-jets}}$	> 160	–
(Small Δm)	$E_{\mathrm{T}}^{\text{miss}}$	> 350	> 350
	$m_{\text{eff}}^{\text{incl}}$	> 1000	> 1000

Table 3: Definitions of the Gtt 1-lepton SRs and CRs of the cut-and-count analysis. All kinematic variables are expressed in GeV except $\Delta\phi_{\min}^{4j}$, which is in radians. The jet p_{T} requirement is also applied to b-tagged jets.

SRs probing the Gtt model in 0-lepton channel are described in Table 4. They follow a similar strategy as for the Gtt 1-lepton regions above. Background composition studies performed on simulated event samples show that semileptonic $t\bar{t}$ events, for which the lepton is out of acceptance or is a hadronically decaying τ-lepton, dominate in the SRs. Thus, CRs to normalise the $t\bar{t}$ +jets background make use of the 1-lepton channel, requiring the presence of exactly one signal lepton. An inverted selection on m_T is applied to suppress overlaps with the 1-lepton SRs. The background prediction is validated in a 0-lepton region, inverting the M_J^Σ selection to suppress any overlap with the SRs.

Regions targeting the Gbb model are presented in Table 5. The region definition follows the same pattern as for Gtt-0L regions, in particular for regions A–C. For very small values of Δm, the Gbb signal does not lead to a significant amount of E_T^{miss}, except if a hard ISR jet recoils against the the gluino pair. Such events are targeted by region D that identifies an ISR-jet candidate as a non-b-tagged high-p_T leading jet (j_1), with a large azimuthal separation $\Delta\phi^{j_1}$ with respect to $\vec{p}_T^{\,miss}$. Similarly, the normalisation of the $t\bar{t}$ background is performed in a 1-lepton CR, to which an inverted selection on m_T is applied to suppress the overlaps with Gtt 1-lepton SRs and the corresponding signal contamination. 0-lepton VRs are constructed in the 0-lepton channel with selections very close to the SR ones. They are mutually exclusive due to an inverted E_T^{miss} selection in the VR.

7.2 Multi-bin analysis

Figures 3 and 4 show that a good separation between signal and background can be achieved with various kinematic variables. The distribution of N_{jet} and m_{eff} for different signal benchmarks and Δm values is used to build a two-dimensional slicing of the phase space in a set of non-overlapping SRs, CRs and VRs that can be statistically combined. The slicing scheme is presented in Figure 5.

The low-N_{jet} region probes especially Gbb-like models, for which the number of hard jets is lower than decay topologies containing top quarks. This category of events will thus only be considered in the
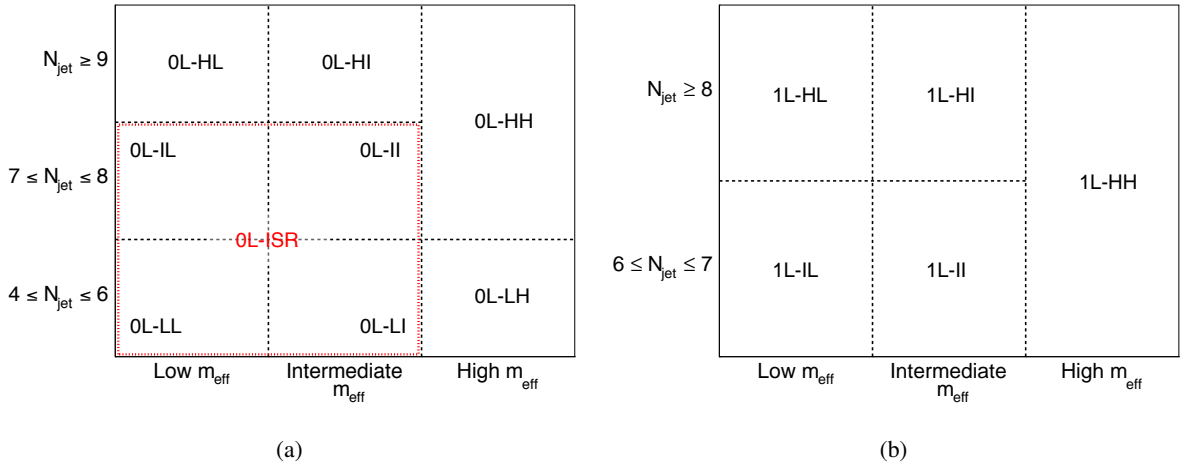
Figure 5: Scheme of the multi-bin analysis for the (a) 0-lepton and (b) 1-lepton regions. The name of the regions is also displayed: "H" stands for "high", "I" for "intermediate" and "L" for "low". The first letter describes the jet multiplicity bin, while the second defines the m_{eff} bin. In the 0-lepton channel, the 0L-ISR region is represented in red. It is a subset of IL, LL, II and LI regions, and maintained mutually exclusive with them as detailed in the text.

0-lepton channel. Gtt events are mostly expected in the high-N_{jet} bin. The intermediate jet multiplicity bin is built to be sensitive to decay topologies with intermediate number of top quarks between Gbb and Gtt, but also to Gbb (with additional jets originating from radiation) and to Gtt (when some jets can fall out of acceptance). The m_{eff} bins are chosen to provide sensitivity to various kinematic regimes: the low-m_{eff} regions are essentially sensitive to soft signals (low Δm), while the high-m_{eff} regions are designed to select highly boosted events.

For each N_{jet}-m_{eff} region presented in Figure 5, the selection has been optimized over all the other variables to maximize the exclusion power for the Gbb and Gtt models. For each m_{eff} bin, a targeted range of Δm has been used in the optimization procedure.

The high and intermediate-N_{jet} regions are presented in Tables 6 and 7. For each m_{eff} region, 0- and 1-lepton channels are used to provide sensitivity to the Gtt model and the decay topologies of the variable branching ratio model that contain at least one top quark. In the intermediate N_{jet} categories the leading jet is required to be b-tagged or the value of $\Delta\phi^{j_1}$ to be lower than 2.9 in order to ensure they are mutually exclusive with the 0L-ISR regions. Both 0-lepton and 1-lepton SRs share a single CR, hosted in the 1-lepton channel, after the application of an inverted m_T selection to suppress the overlap with the 1-lepton SRs. The other kinematic requirements are kept close to the ones of the SR. One VR is defined for each SR in the corresponding lepton channel. Full independence between the signal and VRs is guaranteed by E_T^{miss} and $m_{T,\text{min}}^{b\text{-jets}}$ requirements.

The low-N_{jet} regions are presented in Table 8. Targeting in particular the Gbb model, the transverse momentum of the fourth jet is required to be larger than 90 GeV in all SRs. In the intermediate and low m_{eff} regions, the leading jet is required to be b-tagged or the value of $\Delta\phi^{j_1}$ to be lower than 2.9 in order to be mutually exclusive with the 0L-ISR regions. The $t\bar{t}$ background is dominating in all regions, and is normalized in dedicated 1-lepton regions, defined with a low m_T requirement, as done for the regions of the cut-and-count analysis. VRs are constructed in the 0-lepton channel, reproducing similar background composition and kinematics as in the SR events.

A dedicated set of regions is designed to target very compressed Gbb scenarios in which a hard ISR jet is recoiling the gluino pair. The definition of these regions is presented in Table 9.

Criteria common to all Gtt 0-lepton regions: $p_T^{\text{jet}} > 30$ GeV			
	Variable	SR	CR
Criteria common to all regions of the same type	N_{lepton}	$= 0$	$= 1$
	$\Delta\phi_{\min}^{4j}$	> 0.4	–
	m_T	–	< 150
Region A (Large Δm)	$m_{T,\min}^{b\text{-jets}}$	> 60	–
	$N_{b\text{-jets}}$	≥ 3	≥ 3
	N_{jet}	≥ 7	≥ 6
	E_T^{miss}	> 350	> 275
	$m_{\text{eff}}^{\text{incl}}$	> 2600	> 1800
	M_J^{Σ}	> 300	> 300
Region B (Moderate Δm)	$m_{T,\min}^{b\text{-jets}}$	> 120	–
	$N_{b\text{-jets}}$	≥ 3	≥ 3
	N_{jet}	≥ 7	≥ 6
	E_T^{miss}	> 500	> 400
	$m_{\text{eff}}^{\text{incl}}$	> 1800	> 1700
	M_J^{Σ}	> 200	> 200
Region C (Small Δm)	$m_{T,\min}^{b\text{-jets}}$	> 120	–
	$N_{b\text{-jets}}$	≥ 4	≥ 4
	N_{jet}	≥ 8	≥ 7
	E_T^{miss}	> 250	> 250
	$m_{\text{eff}}^{\text{incl}}$	> 1000	> 1000
	M_J^{Σ}	> 100	> 100

Table 4: Definitions of the Gtt 0-lepton SRs and CRs of the cut-and-count analysis. All kinematic variables are expressed in GeV except $\Delta\phi_{\min}^{4j}$, which is in radians. The jet p_T requirement is also applied to b-tagged jets.

	Variable	SR	CR
Criteria common to all Gbb regions: $N_{\text{jet}} \geq 4$, $p_{\text{T}}^{\text{jet}} > 30$ GeV			
Criteria common to all regions of the same type	$N^{\text{Signal Lepton}}$	0	= 1
	$\Delta\phi_{\text{min}}^{4j}$	> 0.4	–
	m_{T}	–	< 150
Region A (Large Δm)	$N_{b\text{-jets}}$	≥ 3	≥ 3
	$E_{\text{T}}^{\text{miss}}$	> 400	> 400
	m_{eff}	> 2800	> 2500
Region B (Moderate Δm)	$N_{b\text{-jets}}$	≥ 4	≥ 4
	$E_{\text{T}}^{\text{miss}}$	> 450	> 300
	$m_{\text{T,min}}^{b\text{-jets}}$	> 90	–
	m_{eff}	> 1600	> 1600
Region C (Small Δm)	$N_{b\text{-jets}}$	≥ 4	≥ 4
	$E_{\text{T}}^{\text{miss}}$	> 450	> 375
	$m_{\text{T,min}}^{b\text{-jets}}$	> 155	–
Region D (Very small Δm)	$N_{b\text{-jets}}$	≥ 3	≥ 3
	$E_{\text{T}}^{\text{miss}}$	> 600	> 600
	$m_{\text{T,min}}^{b\text{-jets}}$	> 100	-
	$p_{\text{T}}^{j_1}$	> 400	> 400
	$j_1 \neq b$	✓	✓
	$\Delta\phi^{j_1}$	> 2.5	> 2.5

Table 5: Definitions of the Gbb SRs and CRs of the cut-and-count analysis. All kinematic variables are expressed in GeV except $\Delta\phi_{\text{min}}^{4j}$, which is in radians. The jet p_{T} requirement is applied to the four leading jets, a subset of which are b-tagged jets. The $j_1 \neq b$ requirement specifies that the leading jet is not b-tagged.

	Criteria common to all high-N_{jet} regions: $N_{b\text{-jets}} \geq 3$			
	Variable	SR-0L	SR-1L	CR
Criteria common to all regions of the same type	N_{lepton}	0	≥ 1	≥ 1
	$\Delta\phi_{\text{min}}^{4j}$	> 0.4	–	–
	m_{T}	–	> 150	< 150
High-m_{eff} (HH) (Large Δm)	N_{jet}	≥ 7	≥ 6	≥ 6
	m_{eff}	> 2500	> 2300	> 2100
	$m_{\text{T,min}}^{b\text{-jets}}$	> 100	> 120	> 60
	$E_{\text{T}}^{\text{miss}}$	> 400	> 500	> 300
Intermediate-m_{eff} (HI) (Intermediate Δm)	N_{jet}	≥ 9	≥ 8	≥ 8
	m_{eff}	[1800,2500]	[1800,2300]	[1700,2100]
	$m_{\text{T,min}}^{b\text{-jets}}$	> 140	> 140	> 60
	$E_{\text{T}}^{\text{miss}}$	> 300	> 300	> 200
Low-m_{eff} (HL) (Small Δm)	N_{jet}	≥ 9	≥ 8	≥ 8
	m_{eff}	[900,1800]	[900,1800]	[900,1700]
	$m_{\text{T,min}}^{b\text{-jets}}$	> 140	> 140	> 130
	$E_{\text{T}}^{\text{miss}}$	> 300	> 300	> 250

Table 6: Definition of the high-N_{jet} SRs and CRs of the multi-bin analysis. All kinematic variables are expressed in GeV except $\Delta\phi_{\text{min}}^{4j}$, which is in radians.

	Criteria common to all intermediate-N_{jet} regions: $N_{b\text{-jets}} \geq 3$			
	Variable	SR-0L	SR-1L	CR
Criteria common to all regions of the same type	N_{lepton}	0	≥ 1	≥ 1
	$\Delta\phi_{\text{min}}^{4\text{j}}$	> 0.4	–	–
	m_{T}	–	> 150	< 150
	N_{jet}	[7,8]	[6,7]	[6,7]
	$\text{j}_1 = b$ or $\Delta\phi^{\text{j}_1} \leq 2.9$	✓	–	✓
Intermediate-m_{eff} (II) (Intermediate Δm)	m_{eff}	[1600,2500]	[1600,2300]	[1600,2100]
	$m_{\text{T,min}}^{b\text{-jets}}$	> 140	> 140	> 110
	$E_{\text{T}}^{\text{miss}}$	> 300	> 300	> 200
Low-m_{eff} (IL) (Small Δm)	m_{eff}	[800,1600]	[800,1600]	[800,1600]
	$m_{\text{T,min}}^{b\text{-jets}}$	> 140	> 140	> 130
	$E_{\text{T}}^{\text{miss}}$	> 300	> 300	> 300

Table 7: Definition of the intermediate-N_{jet} SRs and CRs of the multi-bin analysis. All kinematic variables are expressed in GeV except $\Delta\phi_{\text{min}}^{4\text{j}}$, which is in radians. The $\text{j}_1 = b$ requirement specifies that the leading jet is b-tagged.

	Criteria common to all low-N_{jet} regions: $N_{b\text{-jets}} \geq 3$		
	Variable	**SR**	**CR**
Criteria common to all regions of the same type	N_{lepton}	0	≥ 1
	$\Delta\phi_{\text{min}}^{4j}$	> 0.4	–
	m_{T}	–	< 150
	N_{jet}	[4,6]	[4,5]
High-m_{eff} (LH) (Large Δm)	m_{eff}	> 2400	> 2100
	$E_{\text{T}}^{\text{miss}}$	> 300	> 200
	$p_{\text{T}}^{j_4}$	> 90	> 30
Intermediate-m_{eff} (LI) (Intermediate Δm)	m_{eff}	[1400,2400]	[1400,2000]
	$j_1 = b$ or $\Delta\phi^{j_1} \leq 2.9$	✓	✓
	$m_{\text{T,min}}^{b\text{-jets}}$	> 140	-
	$E_{\text{T}}^{\text{miss}}$	> 350	> 300
	$p_{\text{T}}^{j_4}$	> 90	> 70
Low-m_{eff} (LL) (Low Δm)	m_{eff}	[800,1400]	[800,1400]
	$j_1 = b$ or $\Delta\phi^{j_1} \leq 2.9$	✓	✓
	$m_{\text{T,min}}^{b\text{-jets}}$	> 140	-
	$E_{\text{T}}^{\text{miss}}$	> 350	> 300
	$p_{\text{T}}^{j_4}$	> 90	> 70

Table 8: Definition of the low-N_{jet} SRs and CRs of the multi-bin analysis. All kinematic variables are expressed in GeV except $\Delta\phi_{\text{min}}^{4j}$, which is in radians. The $j_1 = b$ requirement specifies that the leading jet is b-tagged.

Criteria common to all ISR regions		
$N_{b\text{-jets}} \geq 3$, $\Delta\phi^{j_1} > 2.9$, $p_T^{j_1} > 400$ GeV, $j_1 \neq b$		
Variable	SR	CR
N_{lepton}	0	≥ 1
$\Delta\phi_{\text{min}}^{4j}$	> 0.4	–
m_T	–	> 150
N_{jet}	[4,8]	[4,7]
$m_{T,\text{min}}^{b\text{-jets}}$	> 100	–
E_T^{miss}	> 600	> 400
m_{eff}	< 2200	> 2000

Table 9: Definition of the ISR SR and CR of the multi-bin analysis. All kinematic variables are expressed in GeV except $\Delta\phi_{\text{min}}^{4j}$, which is in radians. The $j_1 \neq b$ requirement specifies that the leading jet is not b-tagged.

8 Systematic uncertainties

The largest sources of detector-related systematic uncertainties in this analysis relate to the jet energy scale (JES), jet energy resolution (JER) and the b-tagging efficiencies and mistagging rates. The JES uncertainties for the small-R jets are derived from $\sqrt{s} = 13$ TeV data and simulations [70], while the JER uncertainties are extrapolated from 8 TeV data using MC simulations. These uncertainties are also propagated to the re-clustered large-R jets, which use them as inputs. The jet mass scale uncertainty has a negligible impact on the re-clustered jets mass. The impact of the JES uncertainties on the expected background yields is between 13% and 25%, while JER uncertainties affect the background yields by 6–16% in the various regions. Uncertainties in the measured b-tagging efficiencies and mistagging rates are the subleading sources of experimental uncertainties. The impact of these uncertainties on the expected background yields is 10–20% depending on the considered region. The uncertainties associated with lepton reconstruction and energy measurements have a negligible impact on the final results. All lepton and jet measurement uncertainties are propagated to the calculation of $E_{\mathrm{T}}^{\mathrm{miss}}$, and additional uncertainties are included in the scale and resolution of the soft term. The overall impact of the $E_{\mathrm{T}}^{\mathrm{miss}}$ soft term uncertainties is also small.

Since the normalisation of the $t\bar{t}$ background is fit in the data CRs, uncertainties in the modelling of this background only affect the extrapolation from the CRs to the SRs and VRs. Hadronisation and parton showering model uncertainties are estimated using a sample generated with Powheg and showered by Herwig++ v2.7.1 with the UEEE5 underlying-event tune. Systematic uncertainties in the modelling of initial- and final-state radiation are explored with Powheg samples showered with two alternative settings of Pythia v6.428. The first of these uses the PERUGIA2012radHi tune and has the renormalization and factorisation scales set to twice the nominal value, resulting in more radiation in the final state. In addition, it has h_{damp} set to $2m_{\mathrm{top}}$. The second sample, using the PERUGIA2012radLo tune, has $h_{\mathrm{damp}} = m_{\mathrm{top}}$ and the renormalisation and factorisation scales are set to half of their nominal values, resulting in less radiation in the event [48]. In each case, the uncertainty is taken as the deviation in the expected yield of $t\bar{t}$ background with respect to the nominal sample. The uncertainty due to the choice of generator is estimated by comparing the expected yields obtained using a $t\bar{t}$ sample generated with MadGraph5_aMC@NLO , and one that is generated with Powheg. Both of these samples are showered with Herwig++ v2.7.1. The total theoretical uncertainty on the inclusive $t\bar{t}$ background is taken as the quadratic sum of these individual components. An additional uncertainty is assigned on the fraction of $t\bar{t}$ events produced in association with additional heavy-flavour jets (i.e. $t\bar{t}+ \geq 1b$ and $t\bar{t}+ \geq 1c$), a process which suffers from large theoretical uncertainties. Simulation studies show that the heavy-flavour fraction in each set of SR, CR and VR, which have the same b-tagged jets requirements, is similar. Therefore, the theoretical uncertainties on this fraction affect these regions in a similar way, and are thus largely cancelled in the semi-data-driven $t\bar{t}$ normalisation based on the observed CR yields. The residual uncertainty on the $t\bar{t}$ prediction is taken as the difference between the nominal $t\bar{t}$ prediction and the one obtained after varying the cross-section of $t\bar{t}$ events with additional heavy-flavor jets by 30%, in accordance with the results of the ATLAS measurement of this cross-section at $\sqrt{s} = 8$ TeV [85]. This component has a negligible contribution (2–5%) to the total impact of the $t\bar{t}$ modelling uncertainties on the background yields, which ranges between 30% and 100% for the various regions. Modelling uncertainties affecting the single-top process especially arise from the interference between the $t\bar{t}$ and Wt processes. This uncertainty is estimated using inclusive $WWbb$ events, generated using MadGraph5_aMC@NLO, which are compared with the sum of $t\bar{t}$ and Wt processes. Furthermore, as for the $t\bar{t}$ modelling uncertainties, variations of Pythia v6.428 settings increasing or decreasing the amount of radiations are also used. Overall, the modelling uncertainties affecting the single-top process lead to changes of 20–100% on the yields in the various regions. An

additional 5% uncertainty is included in the cross-section of single-top processes [86]. Uncertainties on the W/Z+jets backgrounds are estimated varying independently the scales for factorisation, renormalisation and resummation by factors of 0.5 and 2. The scale used for the matching between jets orginating from matrix element and parton shower is also varied. The resulting uncertainties range from 15 to 40% in the various regions. A 50% normalisation uncertainty is assigned to $t\bar{t} + W/Z/h$, $t\bar{t}t\bar{t}$ and diboson backgrounds and are found to have no significant impact on the sensitivity of this analysis. Uncertainties arising from variations in the parton density functions were found to affect background yields by less than 2%, and therefore these uncertainties are neglected here.

The uncertainties in the cross-sections of signal processes are determined from an envelope of different cross-section predictions, as described in Section 4.

Finally, a systematic uncertainty is also assigned on the kinematic correction described in Section 6. The total size of the correction is used as an uncertainty, and is applied to all simulated event samples.

9 Results

The SM background expectation is determined separately in each SR with a profile likelihood fit [87], referred to as background-only fit. The fit uses as a constraint the observed event yield in the associated CR to adjust the $t\bar{t}$ normalisation, assuming that no signal contributes to this yield, and applies that normalisation factor to the number of $t\bar{t}$ events predicted by simulation in the SR. The values of the normalisation factors, the expected background events and observed data yields in all the CRs are shown in Figures 6(a) and 6(b) for the cut-and-count and multi-bin analyses respectively.

The inputs to the fit for each SR are the number of events observed in its associated CR and the number of events predicted by simulation in each region for all background processes. The numbers of observed and predicted events in each CR are described by Poisson probability density functions. The systematic uncertainties in the expected values are included in the fit as nuisance parameters. They are constrained by Gaussian distributions with widths corresponding to the sizes of the uncertainties and are treated as correlated, when appropriate, between the various regions. The product of the various probability density functions forms the likelihood, which the fit maximises by adjusting the $t\bar{t}$ normalisation and the nuisance parameters.

Figures 7(a) and 7(b) show the results of the background-only fit to the CRs, extrapolated to the VRs for the cut-and-count and multi-bin analyses, respectively. The number of events predicted by the background-only fit is compared to the data in the upper panel. The pull, defined by the difference between the observed number of events (n_{obs}) and the predicted background yield (n_{pred}) divided by the total uncertainty (σ_{tot}), is shown for each region in the lower panel. No evidence of significant background mismodelling is observed in the VRs.

The event yields in the SRs for the cut-and-count and multi-bin analyses are presented in Figure 8, where the pull is shown for each region in the lower panel. No significant excess is found above the predicted background. The background is dominated by $t\bar{t}$ events in all SRs. The subdominant background contributions in the 0-lepton regions are $Z(\rightarrow \nu\nu)$+jets and $W(\rightarrow \ell\nu)$+jets events, where for W+jets events the lepton is a unidentified electron or muon or is a hadronically decaying τ-lepton. In the 1-lepton SRs, the subdominant backgrounds are single-top, $t\bar{t}W$ and $t\bar{t}Z$.

24
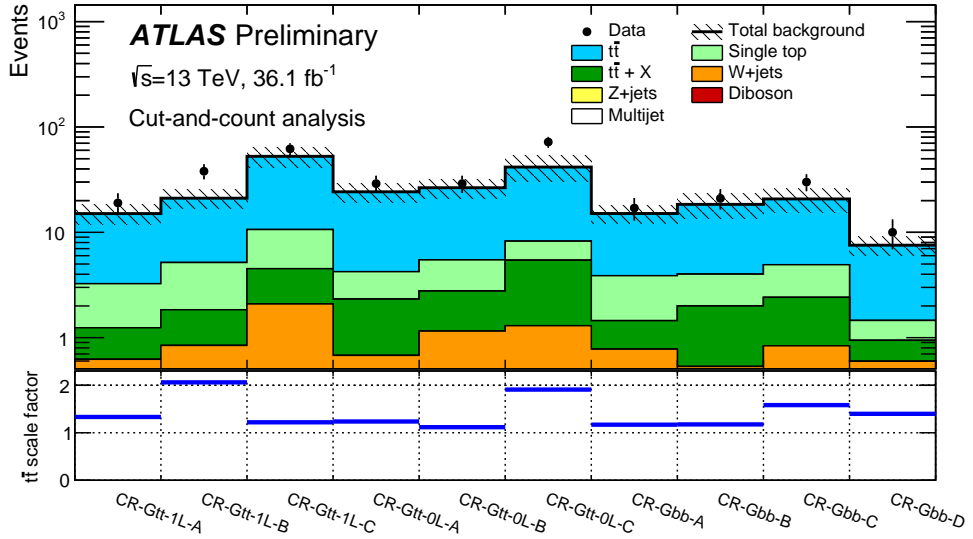
(a)
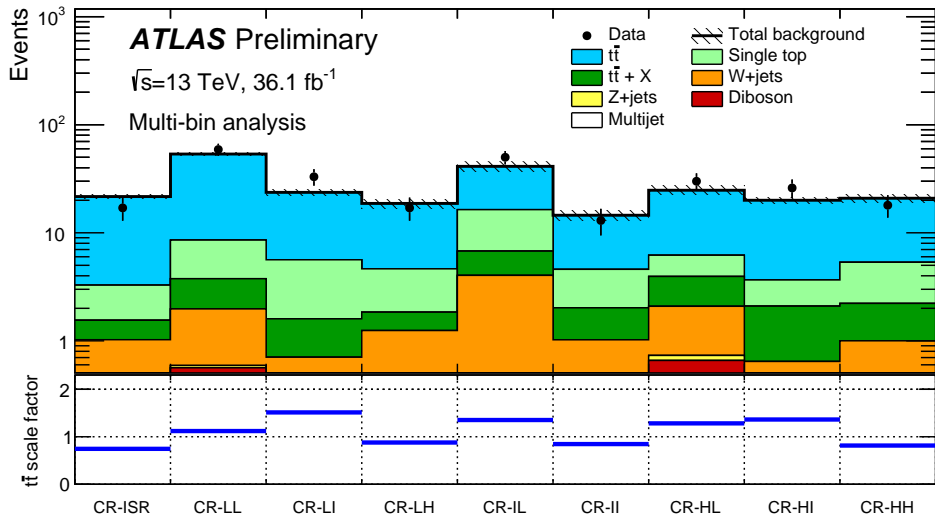
(b)

Figure 6: Inputs and results of the likelihood fit in the control regions of (a) the cut-and-count and (b) the multi-bin analyses. The upper panel shows the observed number of events and the predicted background yield before the fit. The background category $t\bar{t} + X$ includes $t\bar{t}W/Z$, $t\bar{t}h$ and $t\bar{t}t\bar{t}$ events. The $t\bar{t}$ normalization is obtained from the fit and is displayed in the bottom panel.
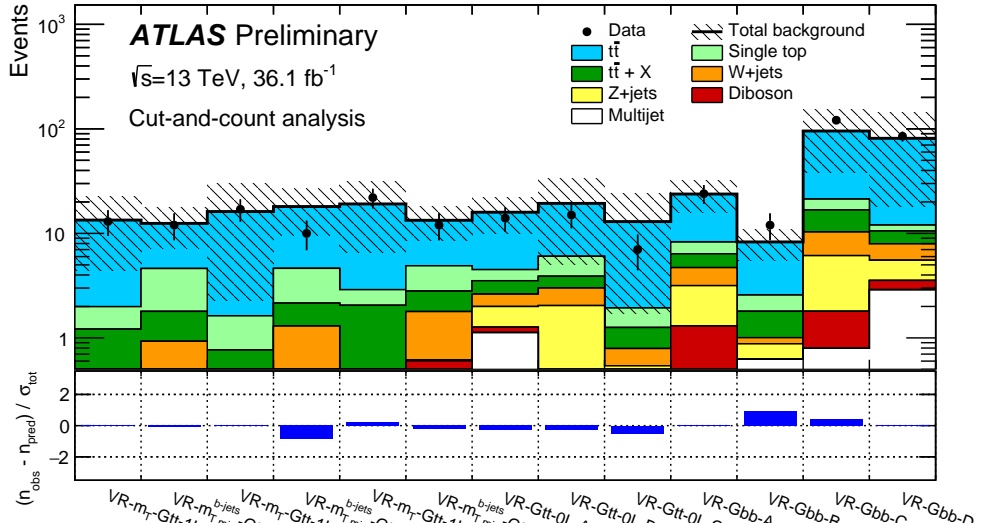
(a)
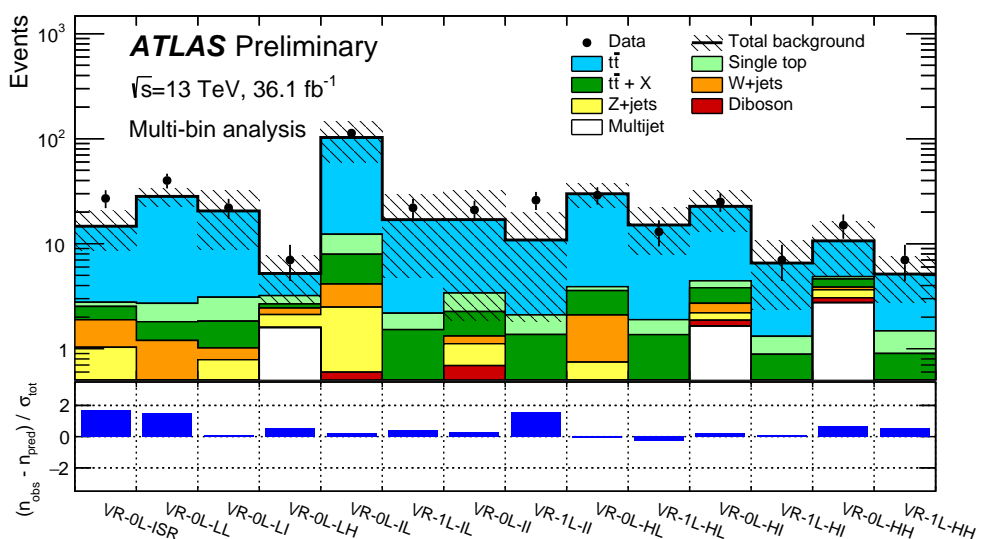
(b)

Figure 7: Results of the likelihood fit extrapolated to the VRs of (a) the cut-and-count and (b) the multi-bin anlayses. The $t\bar{t}$ normalization is obtained from the fit to the CRs. The upper panel shows the observed number of events and the predicted background yield. All uncertainties defined in Section 8 are included in the uncertainty band. The background category $t\bar{t} + X$ includes $t\bar{t}W/Z$, $t\bar{t}h$ and $t\bar{t}t\bar{t}$ events. The lower panel shows the pulls in each VR.
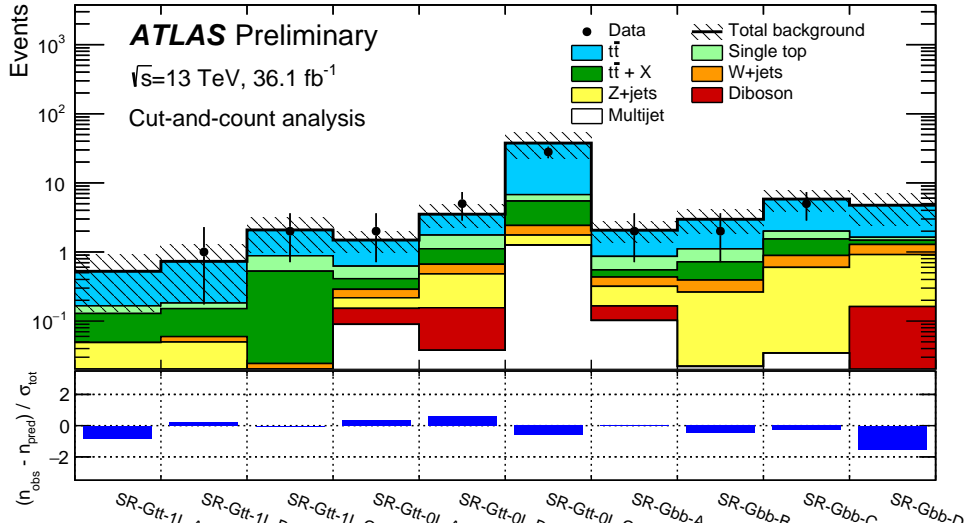
(a)
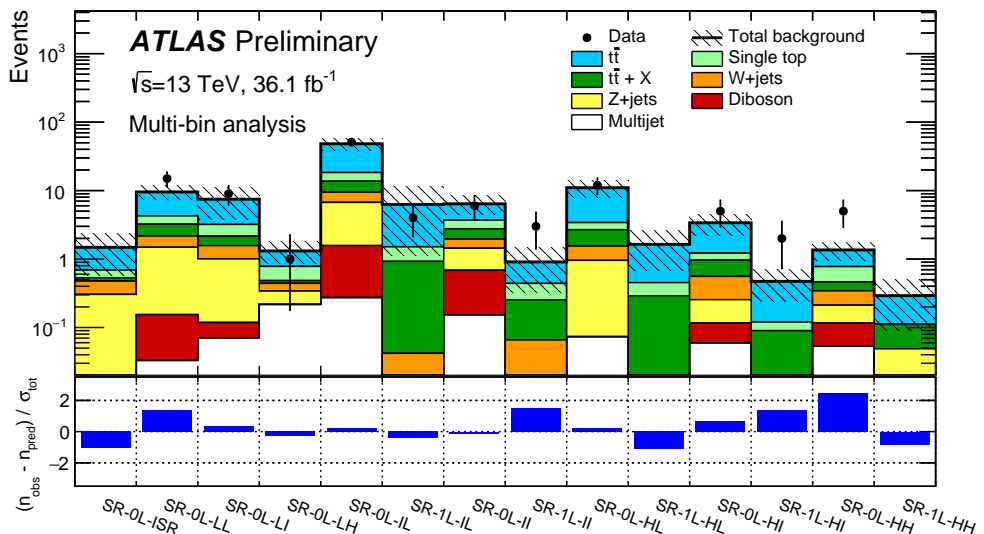
(b)

Figure 8: Results of the likelihood fit extrapolated to the SRs for (a) the cut-and-count and (b) multi-bin analyses. The data in the SRs are not included in the fit. The upper panel shows the observed number of events and the predicted background yield. All uncertainties defined in Section 8 are included in the uncertainty band. The background category $t\bar{t} + X$ includes $t\bar{t}W/Z$, $t\bar{t}h$ and $t\bar{t}t\bar{t}$ events. The lower panel shows the pulls in each SR.

Figure 9 shows the E_T^{miss} distributions in data and simulated samples for SR-Gbb-D, SR-Gtt-1L-A, SR-1L-II and SR-0L-HI and after relaxing the E_T^{miss} threshold to 200 GeV.
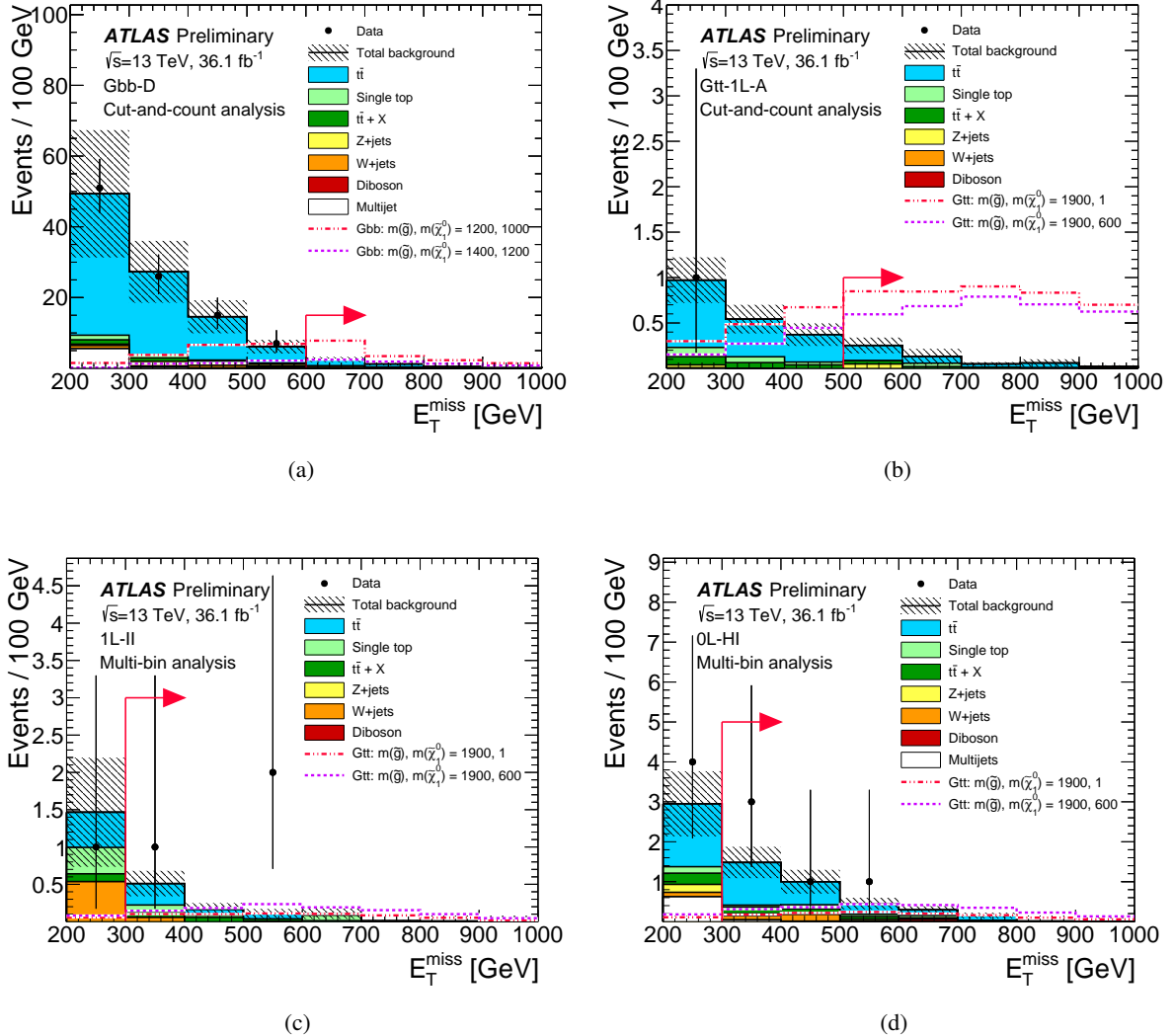

Figure 9: Distributions of E_T^{miss} for (a) SR-Gbb-D, (b) SR-Gtt-1L-A, (c) SR-1L-II and (d) SR-0L-HI. The E_T^{miss} threshold is set to 200 GeV for these plots, with the red lines indicating the threshold values in the actual SRs. The statistical and experimental systematic uncertainties are included in the uncertainty band. The background category $t\bar{t} + X$ includes $t\bar{t}W/Z$, $t\bar{t}h$ and $t\bar{t}t\bar{t}$ events. Two example signal models, normalized according to the theory prediction, are overlaid. The masses of the particles in the legend are in GeV.

Table 10 shows the observed number of events and predicted number of background events from the background-only fit in the Gtt 1-lepton, Gtt 0-lepton and Gbb regions for the cut-and-count analysis. The central value of the fitted background is in general larger than the MC-only prediction. This is in part due to an underestimation of the cross section of $t\bar{t}+ \geq 1b$ and $t\bar{t}+ \geq 1c$ processes in the simulation.

	SR-Gtt-1L		
	A	B	C
Observed events	0	1	2
Fitted background	0.5 ± 0.4	0.7 ± 0.5	2.1 ± 1.1
$t\bar{t}$	0.4 ± 0.4	0.5 ± 0.5	1.2 ± 1.0
Single-top	0.04 ± 0.05	0.03 ± 0.06	0.35 ± 0.18
$t\bar{t} + X$	0.08 ± 0.05	0.09 ± 0.06	0.50 ± 0.28
Z+jets	0.049 ± 0.023	0.050 ± 0.023	< 0.01
W+jets	< 0.01	< 0.01	0.017 ± 0.016
Diboson	< 0.01	< 0.01	< 0.01
MC-only background	0.43	0.45	1.9

	SR-Gtt-0L		
	A	B	C
Observed events	2	5	28
Fitted background	1.5 ± 0.5	3.5 ± 1.3	38 ± 15
$t\bar{t}$	0.9 ± 0.4	1.8 ± 0.7	31 ± 15
Single-top	0.21 ± 0.19	0.64 ± 0.33	1.3 ± 0.7
$t\bar{t} + X$	0.12 ± 0.07	0.45 ± 0.25	3.0 ± 1.6
Z+jets	0.06 ± 0.10	0.3 ± 0.9	0.49 ± 0.31
W+jets	0.07 ± 0.06	0.18 ± 0.15	0.67 ± 0.22
Diboson	0.06 ± 0.07	0.12 ± 0.07	< 0.01
MC-only background	1.3	3.3	23

	SR-Gbb			
	A	B	C	D
Observed events	2	2	5	0
Fitted background	2.1 ± 0.7	3.0 ± 1.1	5.8 ± 2.0	4.7 ± 2.3
$t\bar{t}$	1.2 ± 0.6	1.9 ± 0.9	3.8 ± 1.4	3.1 ± 1.4
Single-top	0.31 ± 0.17	0.4 ± 0.4	0.5 ± 0.5	0.15 ± 0.15
$t\bar{t} + X$	0.12 ± 0.06	0.33 ± 0.19	0.6 ± 0.4	0.19 ± 0.11
Z+jets	0.15 ± 0.34	0.2 ± 0.6	0.6 ± 1.3	0.8 ± 1.9
W+jets	0.12 ± 0.09	0.13 ± 0.12	0.29 ± 0.19	0.37 ± 0.30
Diboson	0.06 ± 0.04	< 0.01	< 0.01	0.15 ± 0.08
MC-only background	1.9	2.7	4.4	3.9

Table 10: Results of the likelihood fit extrapolated to the Gtt 1-lepton, Gtt 0-lepton and Gbb SRs in the cut-and-count analysis, for total background prediction and breakdown of the main background sources. The uncertainties shown include all systematic uncertainties. The data in the SRs are not included in the fit. The background category $t\bar{t} + X$ includes $t\bar{t}W/Z$, $t\bar{t}h$ and $t\bar{t}t\bar{t}$ events. The row "MC-only background" provides the total background prediction when the $t\bar{t}$ normalisation is obtained from a theoretical calculation [61].

Signal channel	p_0 (Z)	σ_{vis}[fb]	S_{obs}^{95}	S_{exp}^{95}
SR-Gtt-1L-A	0.50 (0.00)	0.08	3.0	$3.1^{+0.9}_{-0.1}$
SR-Gtt-1L-B	0.34 (0.41)	0.11	3.9	$3.6^{+1.2}_{-0.5}$
SR-Gtt-1L-C	0.50 (0.00)	0.14	4.9	$4.8^{+1.8}_{-1.0}$
SR-Gtt-0L-A	0.32 (0.47)	0.13	4.8	$4.1^{+1.7}_{-0.7}$
SR-Gtt-0L-B	0.25 (0.68)	0.21	7.4	$5.9^{+2.2}_{-1.4}$
SR-Gtt-0L-C	0.50 (0.00)	0.57	20.6	$23.5^{+6.4}_{-5.3}$
SR-Gbb-A	0.50 (0.00)	0.13	4.6	$4.5^{+1.7}_{-0.9}$
SR-Gbb-B	0.50 (0.00)	0.13	4.5	$5.0^{+2.1}_{-1.1}$
SR-Gbb-C	0.50 (0.00)	0.18	6.6	$6.9^{+2.8}_{-1.5}$
SR-Gbb-D	0.50 (0.00)	0.09	3.1	$4.4^{+2.0}_{-1.1}$

Table 11: The p_0-values and Z (the number of equivalent Gaussian standard deviations), the 95% CL upper limits on the visible cross-section (σ_{vis}), defined as the product of acceptance, reconstruction efficiency and production cross-section, and the observed and expected 95% CL upper limits on the number of BSM events (S_{obs}^{95} and S_{exp}^{95}). The maximum allowed p_0-value is truncated at 0.5.

10 Interpretation

Since no significant excess over the expected background from SM processes is observed, the data are used to derive one-sided upper limits at 95% CL. Two levels of interpretation are provided in this note: model-independent exclusion limits and model-dependent exclusion limits set on the Gbb, Gtt and gluino variable branching ratio models.

10.1 Model-independent exclusion limits

Model-independent limits on the number of beyond-the-SM (BSM) events for each SR are derived with pseudoexperiments using the CL_s prescription [88] and neglecting a possible signal contamination in the CR. Only the single-bin regions from the cut-and-count analysis are used for this purpose, to aid in the reintepretation of these limits. Limits are obtained with a fit in each SR which proceeds in the same way as the fit used to predict the background, except that the number of events observed in the SR is added as an input to the fit. Also, an additional parameter for the non-SM signal strength, constrained to be non-negative, is fit. Limits on the signal strength are translated into upper limits on the visible BSM cross-section (σ_{vis}), which is defined as the product of acceptance, reconstruction efficiency and production cross-section. The results are given in Table 11, where the p_0-values, which represent the probability of the SM background alone to fluctuate to the observed number of events or higher, are also provided.

10.2 Model-dependent exclusion limits

The results are used to place exclusion limits on various signal models. The results are obtained using the CL_s prescription in the asymptotic approximation [89]. The signal contamination in the CRs and the

experimental systematic uncertainties in the signal are taken into account for this calculation. All the regions of the multi-bin analysis are statistically combined to set model-dependent upper limits on the Gbb, Gtt and variable branching ratio models.

The 95% CL observed and expected exclusion limits for the Gbb and Gtt models are shown in the LSP and gluino mass plane in Figures 10(a) and 10(b), respectively. The $\pm 1\sigma_{\text{theory}}^{\text{SUSY}}$ lines around the observed limits are obtained by changing the SUSY cross-section by one standard deviation ($\pm 1\sigma$), as described in Section 4. The yellow band around the expected limit shows the $\pm 1\sigma$ uncertainty, including all statistical and systematic uncertainties except the theoretical uncertainties in the SUSY cross-section. The increase in integrated luminosity leads to an expected improvement of more than (200 GeV) 300 GeV in the gluino mass sensitivity of the current search compared to the previous results [14], assuming massless LSPs in the Gbb (Gtt) models. Gluinos with masses below 1.92 (1.97) TeV are excluded at 95% CL for neutralino masses lower than 300 GeV in the Gbb (Gtt) model. The observed limit for the Gtt model at high gluino mass is significantly weaker than the expected limits due to the mild excesses observed in the signal regions SR-0L-HH and SR-1L-HI of the multi-bin fit analysis. The best exclusion limit on the LSP mass is approximately 1.19 (1.20) TeV, which is reached for a gluino mass of approximately 1.68 (1.40) TeV for Gtt and Gbb models, respectively.


(a)   (b)
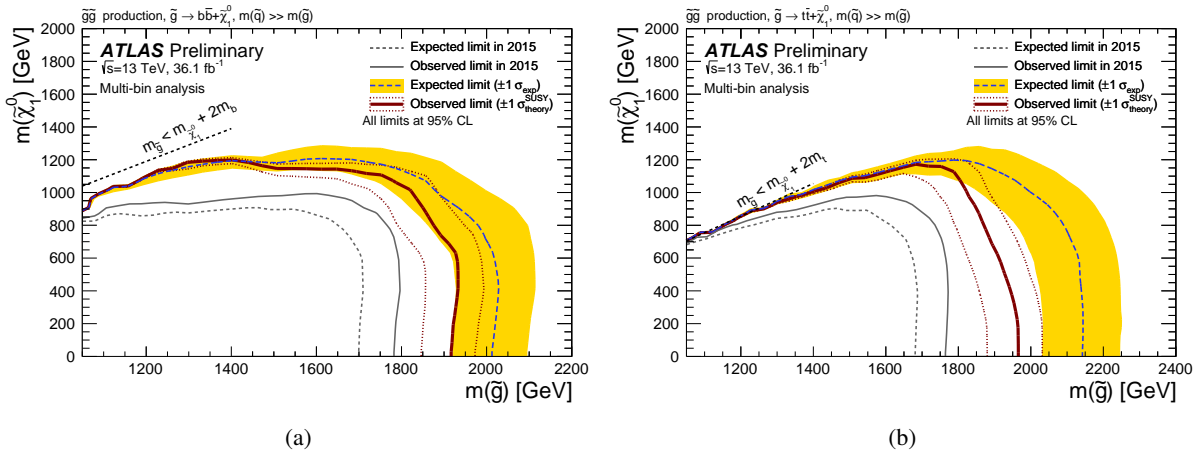
Figure 10: Exclusion limits in the $\tilde{\chi}_1^0$ and $\tilde{g}$ mass plane for (a) the Gbb and (b) the Gtt models obtained in the context of the multi-bin analysis. The dashed and solid bold lines show the 95% CL expected and observed limits, respectively. The shaded bands around the expected limits show the impact of the experimental and background theoretical uncertainties. The dotted lines show the impact on the observed limit of the variation of the nominal signal cross-section by $\pm 1\sigma$ of its theoretical uncertainty. The 95% CL expected and observed limits from the ATLAS search based on 2015 data [14] are also shown.

Limits are also set in the signal model described in Section 2 for which the branching ratios of the gluinos to $tb\tilde{\chi}_1^\pm$ (with $\tilde{\chi}_1^\pm \rightarrow f\bar{f}'\tilde{\chi}_1^0$), $t\bar{t}\tilde{\chi}_1^0$, and $b\bar{b}\tilde{\chi}_1^0$ are allowed to vary, with a unitarity constraint applied on the sum of the three branching ratios. For a $m(\tilde{\chi}_1^0) = 1$ GeV, all branching ratio configurations are excluded at 95% CL for a gluino with a mass of 1.5 TeV, while no configuration is excluded for a hypothesis of $m(\tilde{g}) = 2.1$ TeV, despite an expected exclusion at 95% CL for BR($\tilde{g} \rightarrow t\bar{t}\tilde{\chi}_1^0$) > 75%. For an intermediate gluino mass of 1.9 TeV, this analysis is expected to be sensitive to most of the configuration, except for BR($\tilde{g} \rightarrow tb\tilde{\chi}_1^0$) > 10%. Nevertheless, due to the mild excess observed in SR-0L-HH and SR-1L-HI, the observed limits are looser and all configurations in which BR($\tilde{g} \rightarrow tb\tilde{\chi}_1^0$) < 40% are excluded.

11 Conclusion

A search for pair-produced gluinos decaying via sbottom or stop is presented. LHC proton–proton collision data from the full 2015 and 2016 data-taking periods are analysed, corresponding to an integrated luminosity of 36.1 fb^{-1} collected at $\sqrt{s} = 13$ TeV by the ATLAS detector. The search makes use of several signal regions designed for different scenarios of gluino and LSP masses. The signal regions require several high-p_{T} jets, of which at least three must be b-tagged, large $E_{\mathrm{T}}^{\mathrm{miss}}$ and either zero or at least one charged lepton. Two strategies are employed: one in which the signal regions are optimised for discovery, and another one in which several non-overlapping signal regions are fitted simultaneously to achieve optimal exclusion limits for benchmark signals. For all signal regions, the background is generally dominated by $t\bar{t}$+jets, which is normalised in dedicated control regions. No excess is found above the predicted background in any of the signal regions. Model-independent limits are set on the visible cross-section for new physics processes. Exclusion limits are set on gluino and LSP masses in two simplified models where the gluino decays exclusively as $\tilde{g} \to b\bar{b}\tilde{\chi}_1^0$ or $\tilde{g} \to t\bar{t}\tilde{\chi}_1^0$. For LSP masses below approximately 300 GeV, gluino masses of less than 1.92 TeV and 1.97 TeV are excluded at the 95% CL for the $\tilde{g} \to b\bar{b}\tilde{\chi}_1^0$ and $\tilde{g} \to t\bar{t}\tilde{\chi}_1^0$ models, respectively. These results significantly extend the exclusion limits obtained with the sole 2015 dataset. The results are also interpreted in a model with variable gluino branching ratios to $\tilde{g} \to b\bar{b}\tilde{\chi}_1^0$, $\tilde{g} \to tb\tilde{\chi}_1^0$ and $\tilde{g} \to t\bar{t}\tilde{\chi}_1^0$. For example, a mass point with $m_{\tilde{g}} = 1.9$ TeV and $m_{\tilde{\chi}_1^0} = 1$ GeV is excluded at the 95% CL only if BR($\tilde{g} \to tb\tilde{\chi}_1^0$) < 40%.

References

[1] Yu. A. Golfand and E. P. Likhtman,
Extension of the Algebra of Poincare Group Generators and Violation of p Invariance,
JETP Lett. **13** (1971) 323, [Pisma Zh. Eksp. Teor. Fiz.13,452(1971)].

[2] D. V. Volkov and V. P. Akulov, *Is the Neutrino a Goldstone Particle?*, Phys. Lett. B **46** (1973) 109.

[3] J. Wess and B. Zumino, *Supergauge Transformations in Four-Dimensions*,
Nucl. Phys. B **70** (1974) 39.

[4] J. Wess and B. Zumino, *Supergauge Invariant Extension of Quantum Electrodynamics*,
Nucl. Phys. B **78** (1974) 1.

[5] S. Ferrara and B. Zumino, *Supergauge Invariant Yang-Mills Theories*,
Nucl. Phys. B **79** (1974) 413.

[6] A. Salam and J. A. Strathdee, *Supersymmetry and Nonabelian Gauges*,
Phys. Lett. B **51** (1974) 353.

[7] G. R. Farrar and P. Fayet, *Phenomenology of the Production, Decay, and Detection of New Hadronic States Associated with Supersymmetry*, Phys. Lett. B **76** (1978) 575.

[8] N. Sakai, *Naturalness in Supersymmetric Guts*, Z. Phys. C **11** (1981) 153.

[9] S. Dimopoulos, S. Raby and F. Wilczek, *Supersymmetry and the Scale of Unification*,
Phys. Rev. D **24** (1981) 1681.

[10] L. E. Ibanez and G. G. Ross, *Low-Energy Predictions in Supersymmetric Grand Unified Theories*,
Phys. Lett. B **105** (1981) 439.

[11] S. Dimopoulos and H. Georgi, *Softly Broken Supersymmetry and SU(5)*,
Nucl. Phys. B **193** (1981) 150.

[12] R. Barbieri and G. F. Giudice, *Upper Bounds on Supersymmetric Particle Masses*,
Nucl. Phys. B **306** (1988) 63.

[13] ATLAS Collaboration, *The ATLAS Experiment at the CERN Large Hadron Collider*,
JINST **3** (2008) S08003.

[14] ATLAS Collaboration,
Search for pair production of gluinos decaying via stop and sbottom in events with b-jets and large missing transverse momentum in pp collisions at $\sqrt{s}$ = 13 TeV with the ATLAS detector,
Phys. Rev. D **94** (2016) 032003, arXiv: 1605.09318 [hep-ex].

[15] ATLAS Collaboration, *Search for supersymmetry at $\sqrt{s}$ = 13 TeV in final states with jets and two same-sign leptons or three leptons with the ATLAS detector*, Eur. Phys. J. C **76** (2016) 259,
arXiv: 1602.09058 [hep-ex].

[16] CMS Collaboration,
Inclusive search for supersymmetry using razor variables in pp collisions at $\sqrt{s}$ = 13 TeV,
Phys. Rev. D **95** (1 2017) 012003, arXiv: 1609.07658 [hep-ex].

[17] CMS Collaboration, *Search for supersymmetry in the multijet and missing transverse momentum final state in pp collisions at 13 TeV*, Phys. Lett. B **758** (2016) 152,
arXiv: 1602.06581 [hep-ex].

[18] CMS Collaboration, *Search for new physics with the MT2 variable in all-jets final states produced in pp collisions at sqrt(s) = 13 TeV*, (2016), arXiv: 1603.04053 [hep-ex].

[19] CMS Collaboration, *Search for supersymmetry in pp collisions at $\sqrt{s}$ = 13 TeV in the single-lepton final state using the sum of masses of large-radius jets*, JHEP **08** (2016) 122,
arXiv: 1605.04608 [hep-ex].

[20] CMS Collaboration,
Search for new physics in same-sign dilepton events in proton-proton collisions at $\sqrt{s}$ = 13 TeV,
Eur. Phys. J. C **76** (2016) 439, arXiv: 1605.03171 [hep-ex].

[21] CMS Collaboration, *Search for supersymmetry in events with one lepton and multiple jets in proton-proton collisions at $\sqrt{s}$ = 13 TeV*, Phys. Rev. D **95** (2017) 012011,
arXiv: 1609.09386 [hep-ex].

[22] CMS Collaboration, *A search for new phenomena in pp collisions at $\sqrt{s}$ = 13 TeV in final states with missing transverse momentum and at least one jet using the α_T variable*,
Submitted to: Eur. Phys. J. C (2016), arXiv: 1611.00338 [hep-ex].

[23] CMS Collaboration, *Search for supersymmetry in the all-hadronic final state using top quark tagging in pp collisions at $\sqrt{s}$ = 13 TeV*, Submitted to: Eur. Phys. J. C (2017),
arXiv: 1701.01954 [hep-ex].

[24] J. Alwall, P. Schuster and N. Toro,
Simplified Models for a First Characterization of New Physics at the LHC,
Phys. Rev. D **79** (2009) 075020, arXiv: 0810.3921 [hep-ph].

[25] D. Alves et al., *Simplified Models for LHC New Physics Searches*, J. Phys. G **39** (2012) 105005,
arXiv: 1105.2838 [hep-ph].

[26]   ATLAS Collaboration, *Search for strong production of supersymmetric particles in final states with missing transverse momentum and at least three b-jets at $\sqrt{s}$ = 8 TeV proton-proton collisions with the ATLAS detector*, JHEP **10** (2014) 24, arXiv: 1407.0600 [hep-ex].

[27]   ATLAS Collaboration, *Summary of the ATLAS experiment's sensitivity to supersymmetry after LHC Run 1 — interpreted in the phenomenological MSSM*, JHEP **10** (2015) 134, arXiv: 1508.06608 [hep-ex].

[28]   ATLAS Collaboration, *ATLAS Insertable B-Layer Technical Design Report*, ATLAS-TDR-19, 2010, URL: http://cds.cern.ch/record/1291633, *ATLAS Insertable B-Layer Technical Design Report Addendum*, ATLAS-TDR-19-ADD-1, 2012, URL: http://cds.cern.ch/record/1451888.

[29]   ATLAS Collaboration, *Performance of the ATLAS Trigger System in 2015*, Submitted to: Eur. Phys. J. C (2016), arXiv: 1611.09661 [hep-ex].

[30]   ATLAS Collaboration, *Improved luminosity determination in pp collisions at $\sqrt{s}$ = 7 TeV using the ATLAS detector at the LHC*, Eur. Phys. J. C **73** (2013) 2518, arXiv: 1302.4393 [hep-ex].

[31]   ATLAS Collaboration, *2015 start-up trigger menu and initial performance assessment of the ATLAS trigger using Run-2 data*, ATL-DAQ-PUB-2016-001, URL: https://cds.cern.ch/record/2136007/.

[32]   J. Alwall et al., *The automated computation of tree-level and next-to-leading order differential cross sections, and their matching to parton shower simulations*, JHEP **07** (2014) 079, arXiv: 1405.0301 [hep-ph].

[33]   R. D. Ball et al., *Parton distributions with LHC data*, Nucl. Phys. B **867** (2013) 244, arXiv: 1207.1303 [hep-ph].

[34]   T. Sjostrand, S. Mrenna and P. Z. Skands, *A Brief Introduction to PYTHIA 8.1*, Comput. Phys. Commun. **178** (2008) 852, arXiv: 0710.3820 [hep-ph].

[35]   S. Alioli et al., *A general framework for implementing NLO calculations in shower Monte Carlo programs: the POWHEG BOX*, JHEP **06** (2010) 043, arXiv: 1002.2581 [hep-ph].

[36]   H.-L. Lai et al., *New parton distributions for collider physics*, Phys. Rev. D **82** (2010) 074024, arXiv: 1007.2241 [hep-ph].

[37]   P. Artoisenet et al., *Automatic spin-entangled decays of heavy resonances in Monte Carlo simulations*, JHEP **03** (2013) 015, arXiv: 1212.3460 [hep-ph].

[38]   T. Sjostrand, S. Mrenna and P. Z. Skands, *PYTHIA 6.4 Physics and Manual*, JHEP **05** (2006) 026, arXiv: hep-ph/0603175.

[39]   S. Frixione et al., *NLO QCD corrections in Herwig++ with MC@NLO*, JHEP **01** (2011) 053, arXiv: 1010.0568 [hep-ph].

[40]   ATLAS Collaboration, *Modelling of the $t\bar{t}H$ and $t\bar{t}V$ ($V = W, Z$) processes for $\sqrt{s}$ = 13 TeV ATLAS analyses*, ATL-PHYS-PUB-2016-005, URL: https://cds.cern.ch/record/2120826.

[41]   T. Gleisberg et al., *Event generation with SHERPA 1.1*, JHEP **02** (2009) 007, arXiv: 0811.4622 [hep-ph].

[42]   T. Gleisberg and S. Höche, *Comix, a new matrix element generator*, JHEP **12** (2008) 039, arXiv: 0808.3674 [hep-ph].

[43] F. Cascioli, P. Maierhofer and S. Pozzorini, *Scattering Amplitudes with Open Loops*, Phys. Rev. Lett. **108** (2012) 111601, arXiv: 1111.5206 [hep-ph].

[44] S. Schumann and F. Krauss, *A Parton shower algorithm based on Catani-Seymour dipole factorisation*, JHEP **03** (2008) 038, arXiv: 0709.1027 [hep-ph].

[45] S. Höche et al., *QCD matrix elements + parton showers: The NLO case*, JHEP **04** (2013) 027, arXiv: 1207.5030 [hep-ph].

[46] ATLAS Collaboration, *Multi-boson simulation for* 13 *TeV ATLAS analyses*, ATL-PHYS-PUB-2016-002, URL: https://cds.cern.ch/record/2119986.

[47] D. J. Lange, *The EvtGen particle decay simulation package*, Nucl. Instrum. Meth. A **462** (2001) 152.

[48] P. Z. Skands, *Tuning Monte Carlo Generators: The Perugia Tunes*, Phys. Rev. D **82** (2010) 074018, arXiv: 1005.3457 [hep-ph].

[49] ATLAS Collaboration, *ATLAS Pythia 8 tunes to* 7 *TeV data*, ATL-PHYS-PUB-2014-021, URL: https://cds.cern.ch/record/1966419.

[50] S. Gieseke, C. Rohr and A. Siodmok, *Colour reconnections in Herwig++*, Eur. Phys. J. C **72** (2012) 2225, arXiv: 1206.0041 [hep-ph].

[51] G. Watt and R. S. Thorne, *Study of Monte Carlo approach to experimental uncertainty propagation with MSTW 2008 PDFs*, JHEP **08** (2012) 052, arXiv: 1205.4024 [hep-ph].

[52] S. Agostinelli et al., *GEANT4: A simulation toolkit*, Nucl. Instrum. Meth. A **506** (2003) 250.

[53] ATLAS Collaboration, *The ATLAS Simulation Infrastructure*, Eur. Phys. J. C **70** (2010) 823, arXiv: 1005.4568 [hep-ex].

[54] W. Beenakker et al., *Squark and gluino production at hadron colliders*, Nucl.Phys. **B492** (1997) 51, arXiv: hep-ph/9610490 [hep-ph].

[55] A. Kulesza and L. Motyka, *Threshold resummation for squark-antisquark and gluino-pair production at the LHC*, Phys.Rev.Lett. **102** (2009) 111802, arXiv: 0807.2405 [hep-ph].

[56] A. Kulesza and L. Motyka, *Soft gluon resummation for the production of gluino-gluino and squark-antisquark pairs at the LHC*, Phys.Rev. **D80** (2009) 095004, arXiv: 0905.4749 [hep-ph].

[57] W. Beenakker et al., *Soft-gluon resummation for squark and gluino hadroproduction*, JHEP **0912** (2009) 041, arXiv: 0909.4418 [hep-ph].

[58] W. Beenakker et al., *Squark and gluino hadroproduction*, Int.J.Mod.Phys. **A26** (2011) 2637, arXiv: 1105.1110 [hep-ph].

[59] C. Borschensky et al., *Squark and gluino production cross sections in pp collisions at $\sqrt{s} = 13, 14, 33$ and 100 TeV*, Eur. Phys. J. C **74** (2014) 3174, arXiv: 1407.5066 [hep-ph].

[60] ATLAS Collaboration, *Search for squarks and gluinos with the ATLAS detector in final states with jets and missing transverse momentum using 4.7 fb^{-1} of $\sqrt{s} = 7$ TeV proton-proton collision data*, Phys. Rev. **D87** (2013) 012008, arXiv: 1208.0949 [hep-ex].

[61] M. Czakon and A. Mitov,
Top++: A Program for the Calculation of the Top-Pair Cross-Section at Hadron Colliders,
Comput. Phys. Commun. **185** (2014) 2930, arXiv: 1112.5675 [hep-ph].

[62] N. Kidonakis, *Next-to-next-to-leading-order collinear and soft gluon corrections for t-channel single top quark production*, Phys. Rev. D **83** (2011) 091503, arXiv: 1103.2792 [hep-ph].

[63] N. Kidonakis,
Two-loop soft anomalous dimensions for single top quark associated production with a W- or H-,
Phys. Rev. D **82** (2010) 054018, arXiv: 1005.4451 [hep-ph].

[64] N. Kidonakis, *NNLL resummation for s-channel single top quark production*,
Phys. Rev. D **81** (2010) 054028, arXiv: 1001.5034 [hep-ph].

[65] S Heinemeyer et al., *Handbook of LHC Higgs Cross Sections: 3. Higgs Properties: Report of the LHC Higgs Cross Section Working Group*, (2013),
URL: https://cds.cern.ch/record/1559921.

[66] S. Catani et al.,
Vector boson production at hadron colliders: a fully exclusive QCD calculation at NNLO,
Phys. Rev. Lett. **103** (2009) 082001, arXiv: 0903.2120 [hep-ph].

[67] ATLAS Collaboration, *Vertex Reconstruction Performance of the ATLAS Detector at $\sqrt{s}$ = 13 TeV*,
ATL-PHYS-PUB-2015-026, URL: https://cds.cern.ch/record/2037717.

[68] ATLAS Collaboration, *Properties of jets and inputs to jet reconstruction and calibration with the ATLAS detector using proton–proton collisions at $\sqrt{s}$ = 13 TeV*, ATL-PHYS-PUB-2015-036,
URL: https://cds.cern.ch/record/2044564.

[69] M. Cacciari, G. P. Salam and G. Soyez, *The anti-k_t jet clustering algorithm*, JHEP **04** (2008) 063,
arXiv: 0802.1189 [hep-ph].

[70] ATLAS Collaboration, *Jet Calibration and Systematic Uncertainties for Jets Reconstructed in the ATLAS Detector at $\sqrt{s}$ = 13 TeV*, ATL-PHYS-PUB-2015-015,
URL: https://cds.cern.ch/record/2037613.

[71] ATLAS Collaboration, *Jet global sequential corrections with the ATLAS detector in proton–proton collisions at $\sqrt{s}$ = 8 TeV*, ATLAS-CONF-2015-002,
URL: https://cds.cern.ch/record/2001682.

[72] ATLAS Collaboration,
First look at proton–proton collision data at $\sqrt{s}$ = 13 TeV in preparation for a search for squarks and gluinos in events with missing transverse energy, jets, and an isolated electron or muon,
ATL-PHYS-PUB-2015-029, URL: https://cds.cern.ch/record/2037906.

[73] ATLAS Collaboration,
Performance of pile-up mitigation techniques for jets in pp collisions with the ATLAS detector,
(2015), arXiv: 1510.03823 [hep-ex].

[74] ATLAS Collaboration, *Performance of b-Jet Identification in the ATLAS Experiment*,
JINST **11** (2016) P04008, arXiv: 1512.01094 [hep-ex].

[75] ATLAS Collaboration, *Optimisation of the ATLAS b-tagging performance for the 2016 LHC Run*,
ATL-PHYS-PUB-2016-012, URL: https://cds.cern.ch/record/2160731.

[76] B. Nachman et al.,
Jets from Jets: Re-clustering as a tool for large radius jet reconstruction and grooming at the LHC,
JHEP **02** (2015) 075, arXiv: 1407.2922 [hep-ph].

[77] D. Krohn, J. Thaler and L.-T. Wang, *Jet Trimming*, JHEP **02** (2010) 084,
arXiv: 0912.1342 [hep-ph].

[78] ATLAS Collaboration, *Performance of jet substructure techniques for large-R jets in proton–proton collisions at $\sqrt{s}$ = 7 TeV using the ATLAS detector*, JHEP **09** (2013) 076,
arXiv: 1306.4945 [hep-ex].

[79] ATLAS Collaboration, *Performance of jet substructure techniques in early $\sqrt{s}$ = 13 TeV pp collisions with the ATLAS detector*, ATLAS-CONF-2015-035,
URL: https://cds.cern.ch/record/2041462.

[80] ATLAS Collaboration,
Electron identification measurements in ATLAS using $\sqrt{s}$ = 13 TeV data with 50 ns bunch spacing,
ATL-PHYS-PUB-2015-041, URL: https://cds.cern.ch/record/2048202.

[81] ATLAS Collaboration,
Electron and photon energy calibration with the ATLAS detector using LHC Run 1 data,
Eur. Phys. J. C **74** (2014) 3071, arXiv: 1407.5063 [hep-ex].

[82] ATLAS Collaboration, *Muon reconstruction performance of the ATLAS detector in proton–proton collision data at $\sqrt{s}$ = 13 TeV*, Eur. Phys. J. C **76** (2016) 292, arXiv: 1603.05598 [hep-ex].

[83] ATLAS Collaboration, *Expected performance of missing transverse momentum reconstruction for the ATLAS detector at $\sqrt{s}$ = 13 TeV*, ATL-PHYS-PUB-2015-023,
URL: https://cds.cern.ch/record/2037700.

[84] ATLAS Collaboration, *Performance of missing transverse momentum reconstruction with the ATLAS detector in the first proton–proton collisions at $\sqrt{s}$ = 13 TeV*, ATL-PHYS-PUB-2015-027,
URL: https://cds.cern.ch/record/2037904.

[85] ATLAS Collaboration, *Measurements of fiducial cross-sections for $t\bar{t}$ production with one or two additional b-jets in pp collisions at $\sqrt{s}$ = 8 TeV using the ATLAS detector*,
Eur. Phys. J. C **76** (2016) 11, arXiv: 1508.06868 [hep-ex].

[86] P. Kant et al., *HatHor for single top-quark production: Updated predictions and uncertainty estimates for single top-quark production in hadronic collisions*,
Comput. Phys. Commun. **191** (2015) 74, arXiv: 1406.4403 [hep-ph].

[87] M. Baak et al., *HistFitter software framework for statistical data analysis*,
Eur. Phys. J. C **75** (2015) 153, arXiv: 1410.1280 [hep-ex].

[88] A. L. Read, *Presentation of Search Results: The CL(s) Technique*, J. Phys. G **28** (2002) 2693.

[89] G. Cowan et al., *Asymptotic formulae for likelihood-based tests of new physics*,
Eur. Phys. J. C **71** (2011) 1554, arXiv: 1007.1727 [physics.data-an].

Appendix

	Variable	SR	CR	VR-m_T	VR-$m_{T,min}^{b\text{-jets}}$
Criteria common to all Gtt 1-lepton regions: ≥ 1 signal lepton, $p_T^{\text{jet}} > 30\text{GeV}$, $N_{b\text{-jets}} \geq 3$					
Region A (Large Δm)	N_{jet}	≥ 5	$= 5$	≥ 5	> 5
	m_T	> 150	< 150	> 150	< 150
	$m_{T,min}^{b\text{-jets}}$	> 120	$-$	$-$	> 120
	E_T^{miss}	> 500	> 300	> 300	> 400
	$m_{\text{eff}}^{\text{incl}}$	> 2200	> 1700	> 1600	> 1400
	M_J^{Σ}	> 200	> 150	< 200	> 200
Region B (Moderate Δm)	N_{jet}	≥ 6	$= 6$	≥ 6	> 6
	m_T	> 150	< 150	> 200	< 150
	$m_{T,min}^{b\text{-jets}}$	> 160	$-$	$-$	> 140
	E_T^{miss}	> 450	> 400	> 250	> 350
	$m_{\text{eff}}^{\text{incl}}$	> 1800	> 1500	> 1200	> 1200
	M_J^{Σ}	> 200	> 100	< 100	> 150
Region C (Small Δm)	N_{jet}	≥ 7	$= 7$	≥ 7	> 7
	m_T	> 150	< 150	> 150	< 150
	$m_{T,min}^{b\text{-jets}}$	> 160	$-$	< 160	> 160
	E_T^{miss}	> 350	> 350	> 300	> 300
	$m_{\text{eff}}^{\text{incl}}$	> 1000	> 1000	> 1000	> 1000

Table 12: Definitions of the Gtt 1-lepton signal, control and validation regions for the cut-and-count analysis. All kinematic variables are expressed in GeV except $\Delta\phi_{\text{min}}^{4j}$, which is in radians. The jet p_T requirement is also applied to b-tagged jets.

Criteria common to all Gtt 0-lepton regions: $p_{\mathrm{T}}^{\mathrm{jet}} > 30$ GeV				
	Variable	SR	CR	VR
Criteria common to all regions of the same type	N^{lepton}	$= 0$	$= 1$	$= 0$
	$\Delta\phi_{\mathrm{min}}^{4\mathrm{j}}$	> 0.4	$-$	> 0.4
	m_{T}	$-$	< 150	$-$
Region A (Large Δm)	$m_{\mathrm{T,min}}^{b\text{-jets}}$	> 60	$-$	$-$
	$N_{b\text{-jets}}$	≥ 3	≥ 3	≥ 3
	N_{jet}	≥ 7	≥ 6	≥ 6
	$E_{\mathrm{T}}^{\mathrm{miss}}$	> 350	> 275	> 250
	$m_{\mathrm{eff}}^{\mathrm{incl}}$	> 2600	> 1800	> 2000
	M_J^{Σ}	> 300	> 300	< 300
Region B (Moderate Δm)	$m_{\mathrm{T,min}}^{b\text{-jets}}$	> 120	$-$	$-$
	$N_{b\text{-jets}}$	≥ 3	≥ 3	≥ 3
	N_{jet}	≥ 7	≥ 6	≥ 6
	$E_{\mathrm{T}}^{\mathrm{miss}}$	> 500	> 400	> 450
	$m_{\mathrm{eff}}^{\mathrm{incl}}$	> 1800	> 1700	> 1400
	M_J^{Σ}	> 200	> 200	< 200
Region C (Small Δm)	$m_{\mathrm{T,min}}^{b\text{-jets}}$	> 120	$-$	$-$
	$N_{b\text{-jets}}$	≥ 4	≥ 4	≥ 4
	N_{jet}	≥ 8	≥ 7	≥ 7
	$E_{\mathrm{T}}^{\mathrm{miss}}$	> 250	> 250	> 250
	$m_{\mathrm{eff}}^{\mathrm{incl}}$	> 1000	> 1000	> 1000
	M_J^{Σ}	> 100	> 100	< 100

Table 13: Definitions of the Gtt 0-lepton signal, control and validation regions for the cut-and-count analysis. All kinematic variables are expressed in GeV except $\Delta\phi_{\mathrm{min}}^{4\mathrm{j}}$, which is in radians. The jet p_{T} requirement is also applied to b-tagged jets.

Criteria common to all Gbb regions: $N_{\text{jet}} \geq 4$, $p_{\text{T}}^{\text{jet}} > 30$ GeV				
	Variable	SR	CR	VR
Criteria common to all regions of the same type	$N^{\text{Signal Lepton}}$	0	= 1	0
	$\Delta\phi_{\text{min}}^{4j}$	> 0.4	–	> 0.4
	m_{T}	–	< 150	–
Region A (Large Δm)	$N_{b\text{-jets}}$	≥ 3	≥ 3	≥ 3
	$E_{\text{T}}^{\text{miss}}$	> 400	> 400	> 350
	m_{eff}	> 2800	> 2500	$1900 < m_{\text{eff}} < 2800$
Region B (Moderate Δm)	$N_{b\text{-jets}}$	≥ 4	≥ 4	≥ 4
	$E_{\text{T}}^{\text{miss}}$	> 450	> 300	$250 < E_{\text{T}}^{\text{miss}} < 450$
	$m_{\text{T,min}}^{b\text{-jets}}$	> 90	-	> 100
	m_{eff}	> 1600	> 1600	$1600 < m_{\text{eff}} < 1900$
Region C (Small Δm)	$N_{b\text{-jets}}$	≥ 4	≥ 4	≥ 4
	$E_{\text{T}}^{\text{miss}}$	> 450	> 375	$350 < E_{\text{T}}^{\text{miss}} < 450$
	$m_{\text{T,min}}^{b\text{-jets}}$	> 155	-	> 125
Region D (Very small Δm)	$N_{b\text{-jets}}$	≥ 3	≥ 3	≥ 3
	$E_{\text{T}}^{\text{miss}}$	> 600	> 600	$225 < E_{\text{T}}^{\text{miss}} < 600$
	$m_{\text{T,min}}^{b\text{-jets}}$	> 100	-	> 100
	$p_{\text{T}}^{j_1}$	> 400	> 400	> 400
	$j_1 \neq b$	✓	✓	✓
	$\Delta\phi^{j_1}$	> 2.5	> 2.5	> 2.5

Table 14: Definitions of the Gbb signal, control and validation regions for the cut-and-count analysis. All kinematic variables are expressed in GeV except $\Delta\phi_{\text{min}}^{4j}$, which is in radians. The jet p_{T} requirement is applied to the four leading jets, a subset of which are b-tagged jets. The $j_1 \neq b$ requirement specifies that the leading jet is not b-tagged.

	Criteria common to all low-N_{jet} regions: $N_{b\text{-jets}} \geq 3$			
	Variable	SR	CR	VR
Criteria common to all regions of the same type	N^{lepton}	0	≥ 1	0
	$\Delta\phi^{4j}_{\min}$	> 0.4	–	> 0.4
	m_{T}	–	< 150	–
	N_{jet}	[4,6]	[4,5]	[4,6]
High-m_{eff} (LH) (Large Δm)	m_{eff}	> 2400	> 2100	[2000,2400]
	$E_{\text{T}}^{\text{miss}}$	> 300	> 200	> 200
	$p_{\text{T}}^{j_4}$	> 90	> 30	< 90 if $E_{\text{T}}^{\text{miss}}$ < 300
Intermediate-m_{eff} (LI) (Intermediate Δm)	m_{eff}	[1400,2400]	[1400,2000]	[1250,1800]
	$j_1 = b$ or $\Delta\phi^{j_1} \leq 2.9$	✓	✓	✓
	$m_{\text{T,min}}^{b\text{-jets}}$	> 140	-	< 140
	$E_{\text{T}}^{\text{miss}}$	> 350	> 300	> 300
	$p_{\text{T}}^{j_4}$	> 90	> 70	> 90
Low-m_{eff} (LL) (Low Δm)	m_{eff}	[800,1400]	[800,1400]	[800,1250]
	$j_1 = b$ or $\Delta\phi^{j_1} \leq 2.9$	✓	✓	✓
	$m_{\text{T,min}}^{b\text{-jets}}$	> 140	-	< 140
	$E_{\text{T}}^{\text{miss}}$	> 350	> 300	> 300
	$p_{\text{T}}^{j_4}$	> 90	> 70	> 90

Table 15: Definition of the low-N_{jet} control, signal and validation regions for the multi-bin analysis. All kinematic variables are expressed in GeV except $\Delta\phi^{4j}_{\min}$, which is in radians.The $j_1 = b$ requirement specifies that the leading jet is b-tagged.

Criteria common to all intermediate-N_{jet} regions: $N_{b\text{-jets}} \geq 3$

	Variable	SR-0L	SR-1L	CR	VR-0L	VR-1L
Criteria common to all regions of the same type	N^{lepton}	0	≥ 1	≥ 1	0	≥ 1
	$\Delta\phi^{4j}_{\text{min}}$	> 0.4	–	–	> 0.4	–
	m_{T}	–	> 150	< 150	–	> 150
	N_{jet}	[7,8]	[6,7]	[6,7]	[7,8]	[6,7]
	$j_1 = b$ or $\Delta\phi^{j1} \leq 2.9$	✓	–	✓	✓	–
Intermediate-m_{eff} (II) (Intermediate Δm)	m_{eff}	[1600,2500]	[1600,2300]	[1600,2100]	[1450,2000]	[1450,2000]
	$m^{b\text{-jets}}_{\text{T,min}}$	> 140	> 140	> 110	< 140	< 140
	$E^{\text{miss}}_{\text{T}}$	> 300	> 300	> 200	> 300	> 225
Low-m_{eff} (IL) (Small Δm)	m_{eff}	[800,1600]	[800,1600]	[800,1600]	[800,1450]	[800,1450]
	$m^{b\text{-jets}}_{\text{T,min}}$	> 140	> 140	> 130	< 140	< 140
	$E^{\text{miss}}_{\text{T}}$	> 300	> 300	> 300	> 300	> 300

Table 16: Definition of the intermediate-N_{jet} control, signal and validation regions for the multi-bin analysis. All kinematic variables are expressed in GeV except $\Delta\phi^{4j}_{\text{min}}$, which is in radians. The $j_1 = b$ requirement specifies that the leading jet is b-tagged.

Criteria common to all high-N_{jet} regions: $N_{b\text{-jets}} \geq 3$

	Variable	SR-0L	SR-1L	CR	VR-0L	VR-1L
Criteria common to all regions of the same type	N^{lepton}	0	≥ 1	≥ 1	0	≥ 1
	$\Delta\phi^{4j}_{\text{min}}$	> 0.4	–	–	> 0.4	–
	m_{T}	–	> 150	< 150	–	> 150
High-m_{eff} (HH) (Large Δm)	N_{jet}	≥ 7	≥ 6	≥ 6	≥ 7	≥ 6
	m_{eff}	> 2500	> 2300	> 2100	> 2100	> 2100
	$m^{b\text{-jets}}_{\text{T,min}}$	> 100	> 120	> 60	< 100 if $E^{\text{miss}}_{\text{T}} > 300$	< 140 if $m_{\text{eff}} > 2300$
	$E^{\text{miss}}_{\text{T}}$	> 400	> 500	> 300	< 300 if $m^{b\text{-jets}}_{\text{T,min}} > 100$	< 500
Intermediate-m_{eff} (HI) (Intermediate Δm)	N_{jet}	≥ 9	≥ 8	≥ 8	≥ 9	≥ 8
	m_{eff}	[1800,2500]	[1800,2300]	[1700,2100]	[1650,2100]	[1600,2100]
	$m^{b\text{-jets}}_{\text{T,min}}$	> 140	> 140	> 60	< 140 if $E^{\text{miss}}_{\text{T}} > 300$	< 140 if $E^{\text{miss}}_{\text{T}} < 300$
	$E^{\text{miss}}_{\text{T}}$	> 300	> 300	> 200	< 300 if $m^{b\text{-jets}}_{\text{T,min}} > 140$	< 300 if $m^{b\text{-jets}}_{\text{T,min}} > 140$
Low-m_{eff} (HL) (Small Δm)	N_{jet}	≥ 9	≥ 8	≥ 8	≥ 9	≥ 8
	m_{eff}	[900,1800]	[900,1800]	[900,1700]	[900,1650]	[900,1650]
	$m^{b\text{-jets}}_{\text{T,min}}$	> 140	> 140	> 130	< 140	< 140
	$E^{\text{miss}}_{\text{T}}$	> 300	> 300	> 250	> 300	> 225

Table 17: Definition of the high-N_{jet} control, signal and validation regions for the multi-bin analysis. All kinematic variables are expressed in GeV except $\Delta\phi^{4j}_{\text{min}}$, which is in radians.

Criteria common to all ISR regions			
$N_{b\text{-jets}} \geq 3$, $\Delta\phi^{j_1} > 2.9$, $p_T^{j_1} > 400$ GeV, $j_1 \neq b$			
Variable	SR	CR	VR
N^{lepton}	0	≥ 1	0
$\Delta\phi_{\text{min}}^{4j}$	> 0.4	–	> 0.4
m_T	–	> 150	–
N_{jet}	[4,8]	[4,7]	[4,8]
$m_{T,\text{min}}^{b\text{-jets}}$	> 100	–	> 100
E_T^{miss}	> 600	> 400	> 250
m_{eff}	< 2200	> 2000	< 2000

Table 18: Definition of the ISR control, signal and validation regions for the multi-bin analysis. All kinematic variables are expressed in GeV except $\Delta\phi_{\text{min}}^{4j}$, which is in radians. The $j_1 \neq b$ requirement specifies that the leading jet is not b-tagged.